APPLIED SPECTROSCOPY REVIEWS, 31(3), 193-249 (1996)

BIOMEDICAL APPLICATIONS OF INFRARED AND RAMAN MICROSCOPY

VICTOR F. KALASINSKY
Department of Environmental and Toxicologic Pathology
Armed Forces Institute of Pathology
Washington, DC 20306

Disclaimer: The views expressed herein are those of the author and do not necessarily represent those of the Department of the Army or the Department of Defense.

I. INTRODUCTION

The desire to analyze smaller and smaller amounts of material is a common goal as we push the limits of technology in trying to solve chemical and biochemical problems. In gas chromatography, fused-silica capillary columns (0.25 mm) have almost completely replaced larger-bore (1/4 and 1/8-inch) packed columns [1], and as detection limits are reduced in liquid chromatography, microbore columns with inner diameters of 1 mm or less are quickly replacing the more traditional 4-mm columns [2]. Capillary electrophoresis is likewise demonstrating advantages over conventional gel electrophoresis for many applications [3]. Mass spectrometers are now capable of detecting and identifying materials in the picogram to femtogram range [4]. Vibrational spectroscopic measurements which are the subject of this review currently utilize the experience of optical microscopists in configuring instrumentation to analyze extremely small specimens.

In infrared spectroscopy, beam condensers have been commercially available for quite some time for the analysis of small quantities of sample in micro-liquid cells or pressed in KBr "micropellets." Attenuated total reflectance (ATR) accessories which fit in the sample compartment of a spectrometer require solid specimens no larger than perhaps 1 mm [5, 6]. However, as the ensuing discussion will show, the use of microscope accessories has simplified data collection for samples as small as 10 μm.

Raman spectroscopy can also be used to study small specimens, and the laser, with its coherent, polarized, monochromatic radiation, is an excellent light source for Raman spectroscopy [7, 8]. The required volumes for liquids went from tens of milliliters with older light sources to a few microliters with the easily focused laser beams. But when a laser beam is sent through a microscope

objective, particles in the 1-μm range, with masses of a few picograms, can readily be studied.

Infrared and Raman spectroscopy have been applied to the study of biological materials for many years [9-12]. Studies of bulk properties of proteins, enzymes, lipids, viruses, tissue, and other biological materials have been conducted without the necessity of microsocpes. Structural characteristics, physical properties, and physiological transformations are among these subjects. The ability to study solids, liquids (or melts), and solutions make vibrational methods unique in the field of biological spectroscopy. For example, protein secondary structure determines the frequencies of the so-called "amide" bands associated with the peptide linkage, and comparison of crystalline and solution data are used routinely to determine whether there are differences in protein secondary structure as a function of physical state [13]. The effects of temperature or pH can also be monitored readily. Protein folding (and unfolding) characteristics can be studied by using infrared and Raman spectroscopy, as can phase transitions of phospholipid bilayers as a function of temperature and other physical and chemical parameters [14].

These bulk phenomena are used to help understand physiological processes, but there are applications in which microscopic changes are of importance. Wider availability of microscope accessories for infrared and Raman spectrometers has opened new areas of biomedical spectroscopy where small sample quantity had previously been a limiting factor.

It was recognized in early reports of a reflecting microscope being used for infrared spectroscopy that applications to biologically relevant molecules should be an emphasis for the technique [15]. An infrared microscope was commercially available from Perkin-Elmer in the 1950's on a single-beam instrument, but it suffered from the predictable limitation of combining a dispersive spectrometer with an energy-limiting optical accessory like a microscope [16]. Many of these problems were eliminated with the availability of Fourier transform infrared (FT-IR) spectrometers, and additional improvements were realized when the microscopes were designed expressedly for use with FT-IR spectrometers [17]. Initially, optical microscopes were modified to be compatible accessories; now the microscopes are designed with compact FT-IR spectrometers as the accessories.

Optical design and the wavelength dependence of diffraction phenomena through small apertures place a lower limit on the size of a particle which can be

studied spectroscopically [18]. Improved instrumentation has advanced infrared microscopy to the point where spatial resolution to the diffraction limit is possible; 10-μm spatial resolution is almost routine in the mid-infrared region. If this limitation is critical, shorter wavelengths can be utilized, and Raman spectroscopy can provide better than 1-μm resolution because of the laser excitation in the visible region typically at 488 or 514.5 nm.

Commercial Raman microspectrometers have been available for over twenty years. The MOLE (molecular optics laser examiner) Raman microprobe was configured with a variety of illumination and detection schemes (including a television monitor) for geological, archeological, industrial, and biological applications [19-22]. A comparable instrument was developed in the United States at almost the same time [23-28]. The limitations of Raman microspectroscopy include fluorescence and the power densities at the samples when the laser beam is so tightly focused through a microscope objective. Fluorescence is always a potential problem for Raman spectroscopy, and commercial systems employing near-infrared lasers are available with dispersive or Fourier transform detection of Raman signals [29, 30]. With the longer wavelengths for excitation, there is a concommitant loss in the spatial resolution, but this type of trade-off is very common in analytical spectroscopy.

Because of their respective advantages and disadvantages, infrared and Raman microspectroscopy complement one another in the same ways that are well-known for macroscopic sampling. Applications of vibrational microscopy cover many subject areas, and have been discussed in previous review articles, books, and book chapters [28, 31-35]. Predictably, the emphasis for vibration microspectroscopy has been in areas where light microscopy (and electron microscopy) are standard techniques. Examples of significant contributions to solving problems in geology [36, 37], forensics [38, 39], art [40], and polymer science [41, 42] are found throughout the literature. The use of traditional microscopy in biology suggests many opportunities for vibrational microscopy. Applications related to biochemical problems and medical diagnoses have become more common as the spectroscopic technology has progressed and the other applications listed above have been successful. A review of biomedical vibrational microscopy is therefore warranted, and this will be the subject of the remainder of the article. This review is not meant to be exhaustive but rather illustrative of applications in a field that is changing very rapidly.

II. EXPERIMENTAL CONSIDERATIONS

A. FT-IR Microspectroscopy

Infrared absorption for biological molecules or any specimen relates to transitions between vibrational energy levels. The absorption bands in infrared spectra are characteristic of the structural moieties within the sample [43]. The band positions can be used to identify unknown materials, and changes or differences in band positions can be used to identify a biological process. Both of these aspects of infrared microspectroscopy are relevant to the study of biologically important molecules.

All of the infrared microscopes in use today are based on Fourier transform infrared (FT-IR) spectrometers. As indicated earlier, microscopes were initially regarded as accessories to the large, research-grade spectrometers, but current designs combine very compact spectrometers as accessories on microscopes designed for use in the infrared region of the electromagnetic spectrum.

The optical characteristics of an FT-IR spectrometer are well-suited to the needs of an infrared microscope system [6]. The throughput and multiplex advantages that an FT-IR spectrometer exhibits relative to a dispersive IR spectrometer are essential for energy-limited situations such as microscopy if spectra with adequate signal-to-noise ratios (S/N) are to be obtained on a routine basis. Aperturing of the infrared beam (and thereby limiting the amount of source radiation which arrives at the sample) is required to achieve the spatial resolution desired in infrared microspectroscopy.

Mid-infrared wavelengths in the 2.5- to 25-μm range (2500 - 25,000 nm, or 4000 - 400 cm^{-1}) are suitable for identifying structures within molecules and for monitoring structural changes as is often the desire in studies of biological molecules. The desired optical wavelengths and the optical characteristics of the lenses and other components of the microscope determine the spatial resolution which can be achieved before diffraction phenomena reduce the light intensity beyond detectable limits [33, 44]. The practical limit on spatial resolution for typical mid-infrared spectrometers is approximately 10 μm, although there are instances where this limit has been extended to 6 μm with satisfactory results [45].

One of the important considerations in the design of an infrared microscope is that traditional refractive lenses such as those used in optical (visible) microscopy absorb broad regions of mid-infrared light. For this reason, reflective

optics are required, and Schwarschild condensers such as those shown in Figure 1 are used in commercial reflecting microscopes. The optical diagram of a typical infrared microscope operating in the transmission mode is shown in Figure 2. In this configuration a specimen would be mounted on a transmissive substrate and placed at the focus of the microscope. Common substrates for transmission infrared microscopy are barium fluoride and calcium fluoride. For opaque specimens, reflected infrared light would be collected by the same objective which focuses the light on the sample, and additional mirrors direct the reflected light to the detector. The resulting reflectance spectrum can be as useful as a transmission spectrum for sample identification, but the reflectance configuration of the microscope offers an additional sampling option. If a specimen is mounted on a reflective surface, light which travels through the sample can be reflected **back** through the sample and directed to the detector. Because the infrared beam traverses the sample twice in this "reflection-absorption" experiment, the resulting spectrum is equivalent to a transmission spectrum of twice the thickness of the specimen. Gold and palladium coatings on ordinary glass microscope slides were used to demonstrate the utility of this procedure for 5- to 10-μm thick sections of tissue [46], and aluminum-coated slides are currently commercially available.

B. Raman Microspectroscopy

Raman spectroscopy involves inelastic scattering from a molecule which has been irradiated with monochromatic light. The observed shifts in wavelength (or frequency) in the Raman effect correspond to vibrational energies in biological molecules and can, therefore, be compared to infrared spectra.

Raman spectrometers can be configured as FT-IR spectrometers [29, 47] equipped with near infrared laser sources (i.e., 785 nm or 1064 nm) or as more-traditional dispersive monochromators with ultraviolet, visible [7, 10, 48] or near-infrared excitation [49]. The latter can operate in a wavelength scanning mode with single-channel detection (for example, monochromators and photomultiplier tubes) or as a spectrograph which can take advantage of the multiplexing capabilities of multichannel detectors like photodiode array detectors and charge-coupled devices (CCD). A recent direction in multiplex Raman spectrometry is the use of the Hadamard transform in conjunction with dispersive

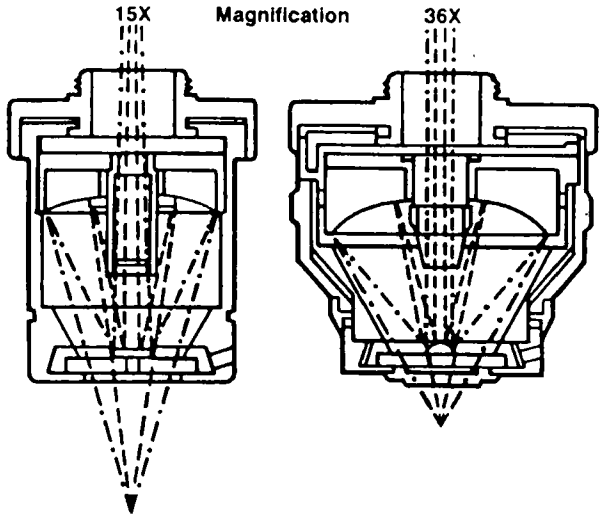

Figure 1. Optical diagram of 15X and 36X reflective microscope objectives. Used by permission, [42].

monochromators and a set of spatial filters [50]. Another aspect of Raman spectroscopy which impacts the ability to obtain spectra of biological molecules is that the wavelengths used are generally compatible with optical fibers [51, 52].

Raman spectroscopy can also benefit from signal enhancement phenomena such as resonance Raman scattering and surface-enhanced Raman scattering [53, 54]. In resonance Raman scattering (RRS), the intensities of selected Raman peaks can be increased if the laser excitation wavelength is within the UV-visible absorption band of a molecule. Intensity changes of three orders of magnitude are possible allowing analysis of low concentrations or the use of extremely low laser power. If a series of different wavelengths is used, the differences in absorption bands of individual molecules to be selectively enhanced, and this process is used in many applications of resonance Raman spectroscopy [53]. In surface-enhanced Raman scattering (SERS), intensities of Raman peaks can be enhanced as a result of interactions between the analyte and a metal surface. Roughened metal surfaces and dispersions of finely divided metal particles (such as copper, silver, and gold) have been used to demmonstrate the principle [54]. As with RRS, SERS can

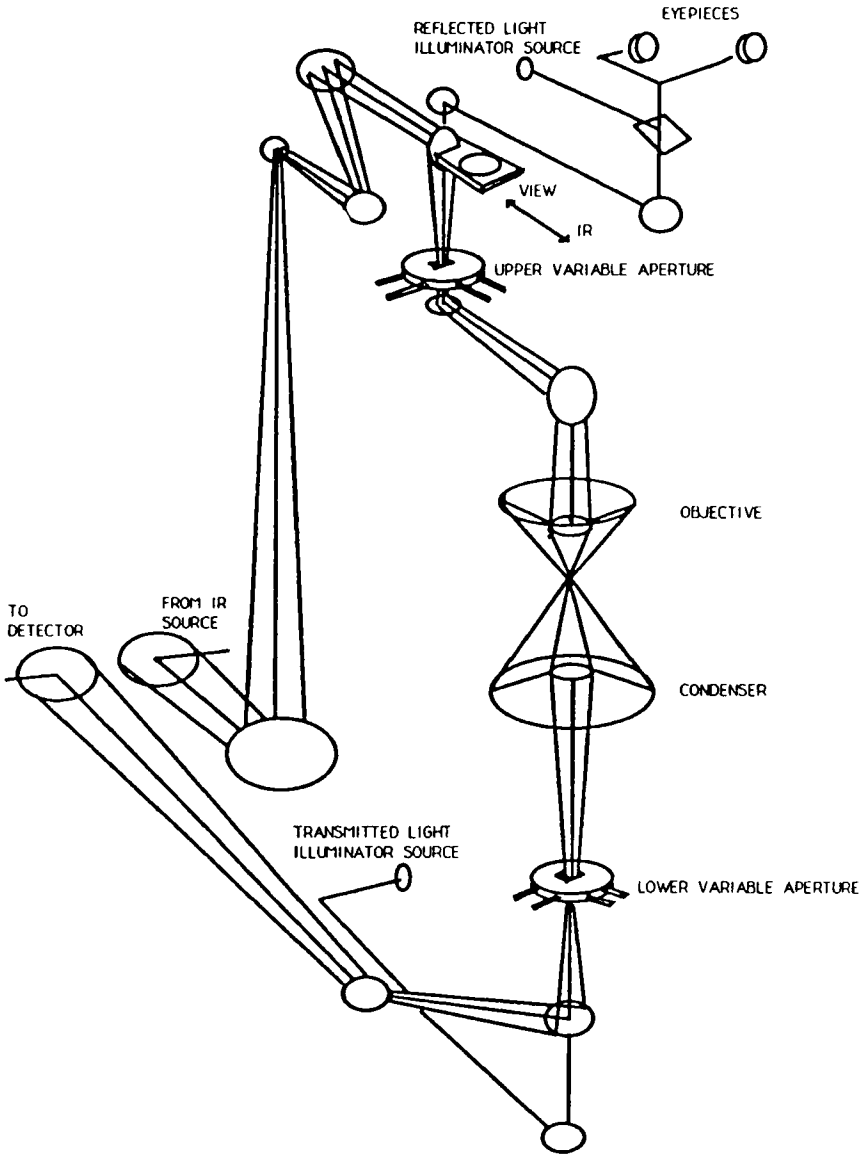

Figure 2. Optical diagram of an FT-IR microscope configured for transmission. Used by permission, [15].

potentially provide a novel approach for obtaining spectra of materials whose spontaneous Raman spectrum is extraordinarily weak.

Laser beams used for excitation in Raman spectroscopy can easily be focused to a spot smaller than 1 mm on the sample, and this approach can provide localized information about a specimen without using microscope optics. However, microscopes have been commercially available on dispersive Raman spectrometers since the early 1970's [19-22]. With excitation from an argon-ion laser (typically 488 or 514.5 nm), spatial resolution better than 1 μm was realized. A generalized schematic of a Raman microscope is shown in Figure 3. The most convenient scattering geometry is 180° so the scattered light is collected by the same microscope objective which delivers the incident laser beam. Various substrates, including sapphire and lithium fluoride, are used for mounting specimens for Raman microscopy [28, 31]. Glass and quartz are also suitable and, of course, are available as microscope slides for normal histopathologic applications. Metal-coated slides (gold or aluminum) are the substrate of choice if the specimen is to be analyzed by using infrared and Raman microscopy. The reflective coating also eliminates any chance of interferences from the glass substrate.

Two problems which can limit the utility of Raman microspectroscopy for biological specimens are fluorescence and the laser power density. Fluorescence intensities can be many orders of magnitude larger than Raman intensities, and a common problem with biological specimens is that fluorescence from trace impurities can overwhelm the Raman signals of the material of interest if the excitation wavelength is of sufficient energy to excite fluorescence. Blue-green (488 and 514.5 nm) excitation generally satisfies this requirement, but it is often possible to quench the fluorescence by prolonged exposure of the specimen to the laser light. If this procedure fails to reduce the fluorescence sufficiently, it may be necessary to use longer wavelength lasers [7, 48]. Infrared lasers with wavelengths as long as 1339 nm have been shown to provide high-quality Raman spectra [29, 50].

High power densities (power per unit area) can lead to sample deterioration even with the laser power in the range of tens of milliwatts. This problem can only be remedied by minimizing laser power and maximizing the optical collection and detection efficiency of the spectrometer. Despite potential limitations of Raman microscopy it is possible to collect spectra of biologically important materials of microscopic sizes [28, 31].

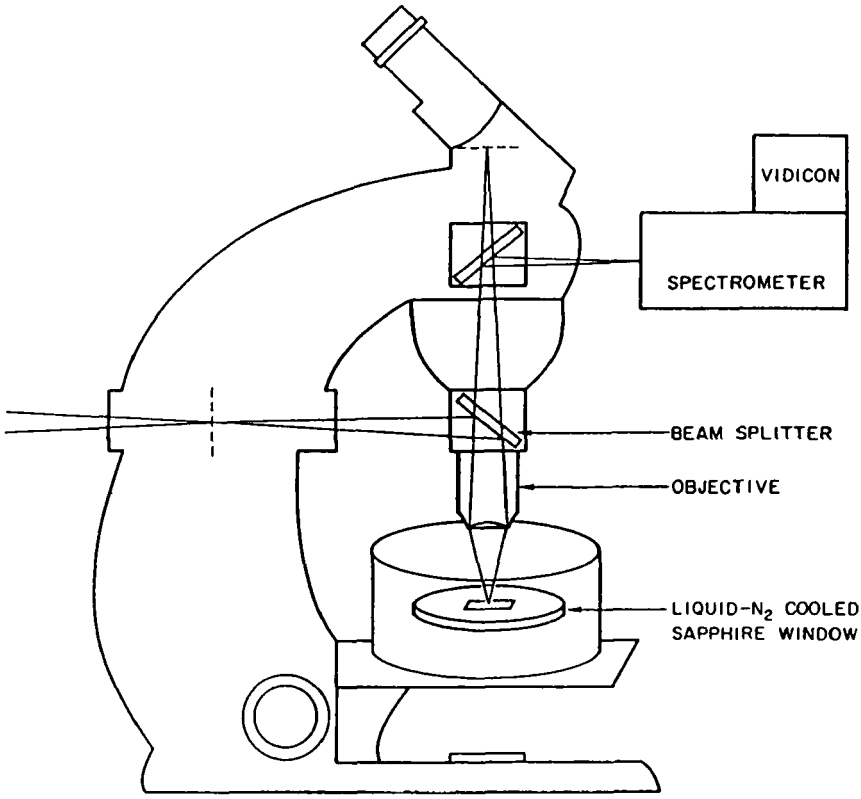

Figure 3. Schematic diagram of a Raman microspectrometer system configured for 180° scattering. Used by permission, [62].

C. Spectral Mapping and Imaging

The importance of the spatial resolution attainable in microspectroscopic experiments relates primarily to the ability to measure spectra of small, isolated regions of specimens and, thereby, to differentiate regions of interest in a specimen. Since vibrational infrared and Raman spectra consist of peaks associated with stretching and bending motions of the structural units within a molecule, bands in a specified wavenumber range can be used to determine regions within a sample where a particular species is located. This "functional

group mapping" procedure requires spectra to be collected at carefully controlled positions in the specimen (micropositioning under computer control) and the necessary software to generate contour plots or axonometric plots. Mapping has been applied successfully to solving problems associated with polymers [56-58]. In biomedical applications, similar information can be obtained, and mapping regions of tissue to identify various "other" materials is a useful approach.

To completely map an area of interst, spectral data must be collected at each position in a two-dimensional grid covering the area. With appropriate software, these data can be displayed with a color scale (or gray scale) to indicate differences in spectral intensities and thereby generate a video image of the sample. In comparing such an image to those obtained digitally or visually from an ordinary (visible) light microscope, the advantage of the infrared or Raman image is that specific structural information is displayed. In biomedical applications where light microscopy and electron microscopy are utilized routinely, the additional information potentially supplied by vibrational images can aid in the interpretation of the data.

An alternative to the time-consuming task of point-by-point mapping is direct imaging using two-dimensional detectors [59, 60]. The concept is outlined in Figure 4 where the images are detected sequentially at λ_0, then λ_1, etc. in real-time as shown. The stored data can be processed to show either a functional group image or, by displaying intensity data at a single pixel location from a series of images, a conventional spectrum.

III. APPLICATIONS OF VIBRATIONAL MICROSPECTROSCOPY

The emphasis in microspectroscopy is generally on small sample sizes, and in biomedical applications the interest is in studying isolated cells, tissue, crystalline materials, and foreign materials in tissue as a means of investigating the details of observations made in bulk materials. Microspectroscopy allows additional information to be obtained from tissue and other specimens prepared for traditional histopathologic examination. The range of examples in biomedical applications related to patient care and diagnosis is quite varied, and hopefully the utility in biomedical applications will be made clear in the following groups of examples.

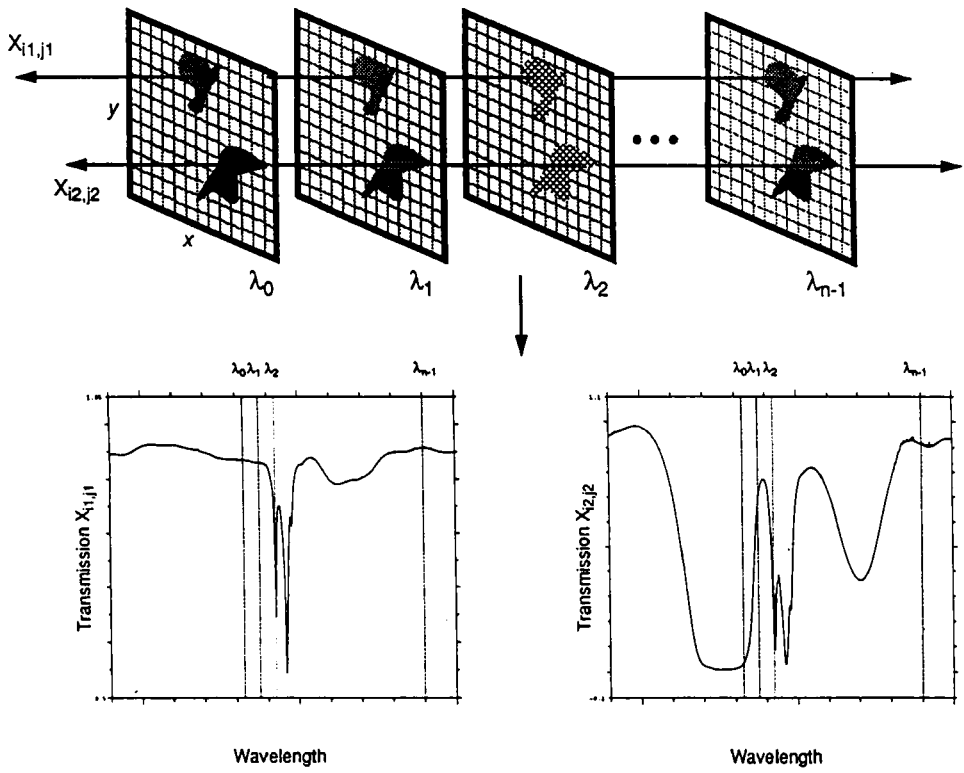

Figure 4. Diagram representative of data collected with an imaging spectrometer. Used by permission, [59].

A. Single Cells

The prospect of using microspectroscopy to monitor dynamic processes or structural changes in individual cells is very attractive. And while macroscopic resonance Raman spectroscopy had been used to study many photoactive processes involved in vision, Mathies and coworkers [61, 62] used a Raman microscope to obtain spectra from single photoreceptor cells as small as 1 x 10 μm mounted on a -196°C cold-stage. For the toad (*Bufo marinus*), 488-nm excitation yielded the spectrum shown in Figure 5b. When a laser beam at 568 nm was

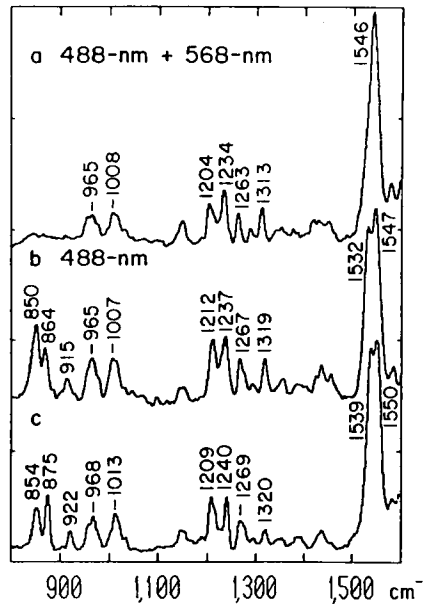

Figure 5. Resonance Raman spectra of visual materials: (a) Toad red rod photoreceptors using a 488-nm probe beam with a coaxial 568-nm pump beam; (b) Toad red rod photoreceptors using a 488-nm probe beam; (c) Bovine visual pigments using a 488-nm probe. Used by permission, [61].

directed at the specimen coaxially with the 488-nm beam, the spectrum in Figure 5a was observed. The 568-nm laser was used to induce the photolysis of the intermediate bathorhodopsin. The decreases in intensities at 850, 864, 915, and 1532 cm^{-1} resulted in these lines being assigned to bathorhodopsin [61]. For comparison, a spectrum of bovine visual pigments is shown in Figure 5c. The intensities between 800 and 900 cm^{-1} for the toad and bovine specimens have been interpreted to mean that their conformations are different because of differences in the attached proteins. Similar studies were conducted with goldfish using 583 nm for Raman excitation. In this case, however, bathorhodopsin concentrations were increased by using a coaxial 482-nm pump. Using these examples, the authors demonstrated photoisomerization inside intact cells without the necessity of

isolating the individual components. This procedure will be useful in elucidating various aspects of the visual process.

Puppels *et al.* described a high-sensitivity confocal Raman microscope designed to obtain spectra of single cells [63-65]. With 660-nm excitation from a dye laser, they were able to achieve a (lateral) spatial resolution of 0.5 μm and a depth resolution of 1.3 μm. The relatively long visible wavelength laser beam greatly reduced the danger of fluorescence and sample degradation during data collection. Figure 6 shows spectra of the nucleus (b) and cytoplasm (a) of an intact human eosinophilic granulocyte and a spectrum of a single chromosome (c). The spectrum of the nucleus is dominated by DNA and protein peaks and is, therefore, very different and distinct from the cytoplasm. The spectra of chromosomes offer an opportunity to characterize the detailed chemical structures associated with chromosomes at the molecular level [63]. Raman spectra of the nuclei of neutrophilic, eosinophilic, abd basophylic granulocytes also exhibit lines associated with DNA and protein, but the cytoplasm of these three types of cells showed distinct differences associated with their individual enzymes [64].

Dong *et al.* recorded infrared microspectra of single red blood cells in H_2O and D_2O through a 10- x 10-μm aperture, and the protein amide-I, amide-II, and amide-III bands were clearly visible [66]. The authors also demonstrated the ability to study ligand-binding by recording spectra of the carbon monoxide complex with individual erythrocytes (both the ^{12}C and ^{13}C derivatives).

Sureau *et al.* utilized ultraviolet excitation to record resonance Raman spectra of single living cells [67]. Cultured T47D human mammary tumor cells exhibited spectra dominated by cellular purines with 257-nm laser radiation. Also observed was evidence of protein amide I and tryptophan residues.

Differences between normal cells and tumors have been studied by using FT-IR, Raman, and many spectroscopic techniques. Wong and coworkers [68-71] have used *macroscopic* sampling to demonstrate the correlations between FT-IR spectral data and histopathologic diagnoses. Macroscopic Raman spectroscopy was used to characterize normal and cancerous breast biopsies [72, 73], and Benedetti and coworkers have used macro- and microscopic FT-IR spectra for a similar purpose [74, 75]. Normal and neoplastic lung cells were physically separated, and relatively homogeneous dispersions of cells were placed on BaF_2 windows. The most striking spectral differences were in the region of the phosphate vibrations associated with DNA. By comparing intensities at 1080 cm^{-1} (DNA) and 1540 cm^{-1} (protein) as indicated in Figure 7, it was possible to

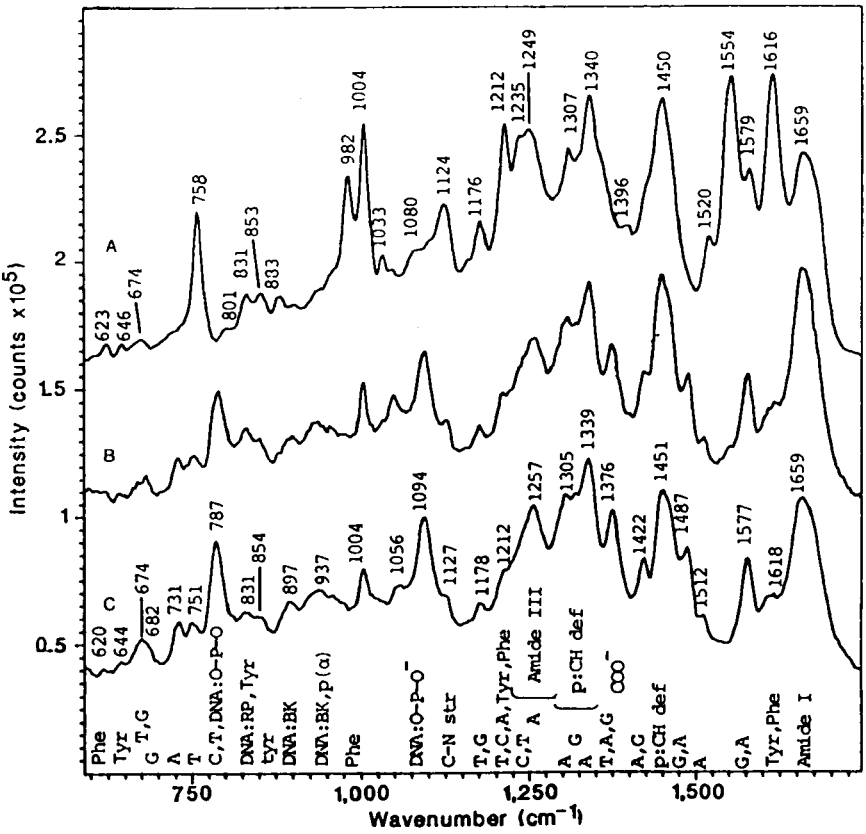

Figure 6. Raman spectra of a single cell and a single chromosome: (A) Spectrum of a cytoplasmic region of a human eosinophilic granulocyte; (B) Spectrum of the nucleus of the same cell; (C) Spectrum of a chromatid of a Chinese hamster lung cell. Used by permission, [63].

distinguish between the normal and tumor cells. Additional work is necessary to determine the extent to which this FT-IR parameter can be used to diagnose the variety of tumors viewed in a pathology laboratory.

Surface-enhanced Raman microscopy of zebrafish eggs was the subject of a study using 532-nm radiation from a Nd:YAG laser [76]. A silver probe with a tip ranging from 1 - 3 μm was used as the SERS substrate. Three regions of the egg

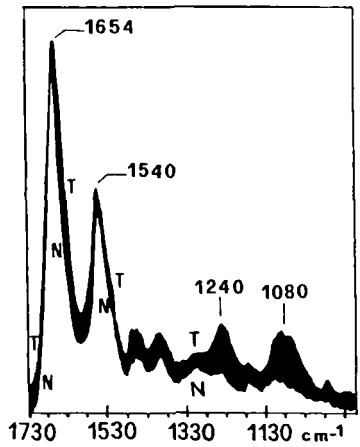

Figure 7. FT-IR spectra of normal (N) lung cells and tumor (T) cells. The darkened area represents spectral differences. Used by permission, [75].

were studied; the outer chorion which is composed primarily of proteins, the yolk which contains carotenoid pigments, and the embryo cells which are made up of peptides and nuceotides.

These studies emphasize the variety of questions which can be probed using microspectroscopy of "single" cells. Superior spatial resolution gives Raman microscopes a distinct advantage over FT-IR microscopes, but there must also be a judicious choice of laser excitation wavelength. For situations in which less spatial resolution is reasonable for viewing groups of similar cells, FT-IR data are adequate and relatively easy to obtain.

B. Bacteria

Single cells or collections of a few cells of chromobacteria provided resonance Raman spectra in a microscope using 488-nm radiation [77, 78]. The 5-μm beam was larger than individual cells, but high-quality resonance-enhanced spectra dominated by lines from carotenoids in the bacteria were recorded. For the highly pigmented strain of *Rhodospirillum*, only 1 - 3 organisms were required

within the focus of the laser; 10 - 12 organisms were required for the lighter colored *Flavobacterium* and *Rhodopseudomonus*. These results provided rapid detection and identification of the bacteria, and it was suggested mixtures of bacteria could likewise be identified.

Macroscopic identification of *Staphylococcus epidermidis* using ultraviolet light at 231.5 nm for resonance enhancement has also been reported. The authors showed that the spectra of live and heat-killed bacteria were different and could be used diagnostically to evaluate bacterial colonies [79].

C. Cardiovascular Pathology

Conventional macroscopic Raman spectra of calcified atherosclerotic plaques in human aorta tissue have been used to demonstrate the presence of hydroxyapatite [80]. Raman microprobe spectra with some limited FT-IR data were collected for calcified atherosclerotic plaques and calcifications on ventricular prostheses implanted in animals [81]. The 514.5-nm argon laser line was focused to 10 μm for the Raman experiments. The authors considered a series of calcium phosphates and calcium phosphate carbonates (carbonate apatites) in interpreting the spectral results. Figure 8 compares Raman spectra of deproteinated aortic plaque and a synthetic carbonate apatite. The phosphate stretch near 960 cm^{-1} is clearly evident, but the intensity near 1075 cm^{-1} (which is comprised of contributions from the phosphate antisymmetric stretch and the carbonate symmetric stretch) was matched by adding approximately 4.3% (by weight) carbonate. Similar results were reported for undeproteinated plaques, and it was suggested that ratios of the these two bands could be used to obtain semiquantitative values of carbonate content of calcified plaques.

In another study, Raman spectra of macroscopic regions of calcified aorta were analyzed using a dispersive instrument with excitation at 741 nm [82]. The laser beam was focused to a spot size of approximately 50 μm for data collection, and fresh-frozen sections of aorta were used in the experiments. Hydroxyapatite was identified on the aorta wall by its strong signal near 960 cm^{-1}, and the authors noted that fluorescence had precluded data collection for their specimens using 514.5-nm excitation. A layer of tissue over the calcified plaque was found to attenuate the Raman signal, but the authors noted that the results were promising for the use of Raman spectroscopy as a guide for laser angioplasty.

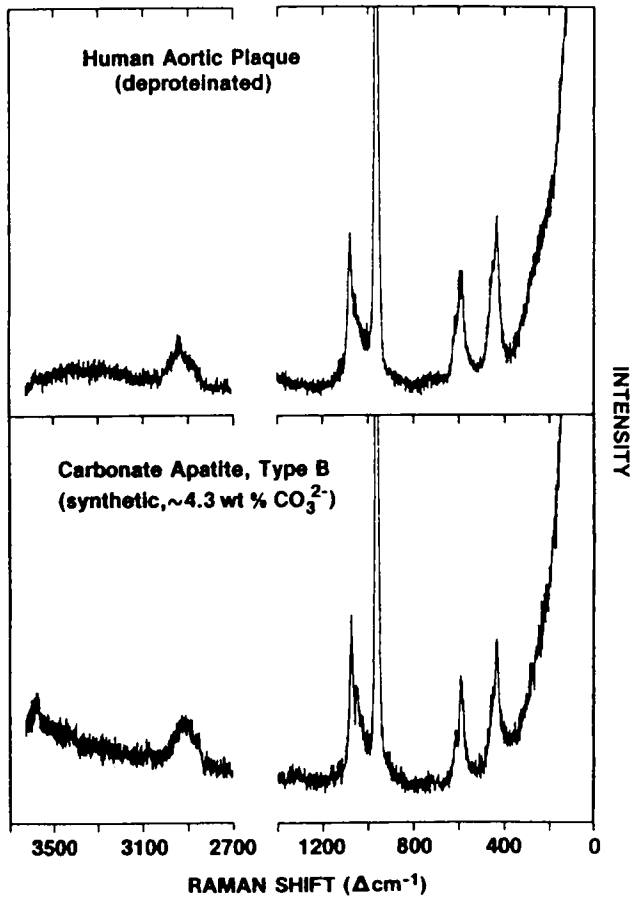

Figure 8. Micro-Raman spectra of a deproteinated human aortic deposit (upper spectrum) and a synthetic carbonate apatite (4.3% carbonate by weight). Used by permission, [81].

FT-Raman spectra, collected with 1064-nm laser output focused to 1.0 mm, were used to study the inner and outer surfaces (intima and adventitia, respectively) of a human aorta [83]. Figure 9 shows spectra of the two surfaces of a normal aorta along with a spectrum of a triglyceride. Histologically, the adventitia was observed to be covered with a layer of adipose tissue, and the similarity between the adipose tissue and triolein is to be expected. A spectrum of a fibrous plaque on the intima is shown in the uppermost protion of Figure 10. Its spectral features are essentially the same as those for a normal aorta (Figure 9) with minor relative intensity differences related to contributions from the different proteinaceous materials comprising the aorta. The atheromatous plaque shown in the middle of Figure 10 is very similar to the cholesterol spectrum below.

Kodali *et al.* employed FT-IR microspectroscopy to map regions of atherosclerotic arteries from two strains of rabbits [84]. Transversely-cut sections of frozen arterial tissue (5 μm thick) were viewed through a 20- x 20-μm aperture to allow the intima (inner wall) and media to be mapped; the adventitia (outer wall) was not studied. Cholesterol and cholesteryl esters were considered important for the study, and spectra of representative authentic specimens are shown in Figure 11.

Spectra of the arterial wall taken from a rabbit with a genetic predisposition to atherosclerosis are shown in Figure 12. Distinct changes in the C-H, =C-H, and C=O stretches were observed at the boundary between the media and intima. The protein amide-I and amide-II bands are prominent in the media as expected for the muscle in this region of the artery wall. The axonometric plots in Figures 13, 14], based on the amide-I and ester C=O vibrations, respectively, provide useful maps of the intima and media. It is also clear that the structure of the plaque in the intima changes as the lumen of the artery is approached. Atherosclerosis was induced in a second strain of rabbits who were fed a cholesterol-rich diet after being subjected to a balloon catheter procedure which damages the endothelial cells on the intimal surface of an artery [84]. Figures 15 and 16, also constructed from the amide-I and C=O stretching regions, show a pattern of protein and esters in the media and intima which is different from that observed for the other strain of rabbits. These data indicate that microscopic studies of this type may be useful in following the progress of atherosclerotic processes.

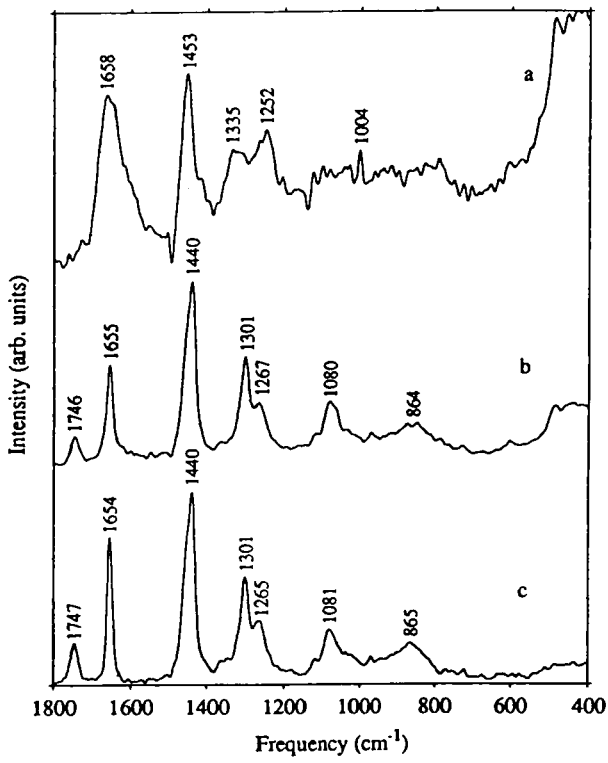

Figure 9. Near infrared Fourier transform Raman spectra of (a) the intimal side of a normal aorta, (b) the adventitial side of a normal aorta, and (c) triolein, a triglyceride. Used by permission, [83].

D. Neuropathology

FT-IR studies of macroscopic quantities of brain tissue (of the order of 1 mm x 1 mm) have been undertaken with the desire to utilize the spectroscopic data diagnostically in multiple sclerosis and Alzheimer's disease [85, 86]. In the former study, changes in lipid content and the lipid/protein ratio were observed between white matter and multiple sclerosis plaques, while water absorption in the vicinity of the amide-I band near 1650 cm^{-1} was suggested as a means for distinguishing

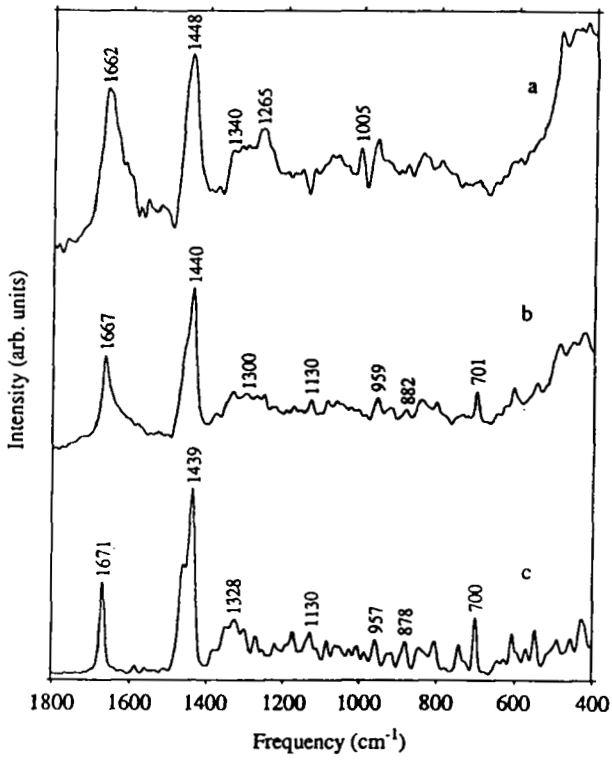

Figure 10. Near infrared Fourier transform Raman spectra of (a) a fibrous plaque, (b) an atheromatous plaque, and (c) cholesterol monohydrate powder. Used by permission, [83].

between gray matter and plaques. In the latter study, infrared spectra were used to demonstrate the deposition of beta-amyloid peptide in brain tissue from Alzheimer's patients. Aggregates of this protein may be linked to its neurotoxicity. Additional work in this area using microspectrocopy techniques to localize these spectral observations appears to be promising.

Wetzel and coworkers have conducted numerous FT-IR microspectroscopy studies of mouse and rat brain tissue [87-91]. Frozen sections of tissue (8 μm thick on BaF_2) were mapped according to the particular emphasis of the study

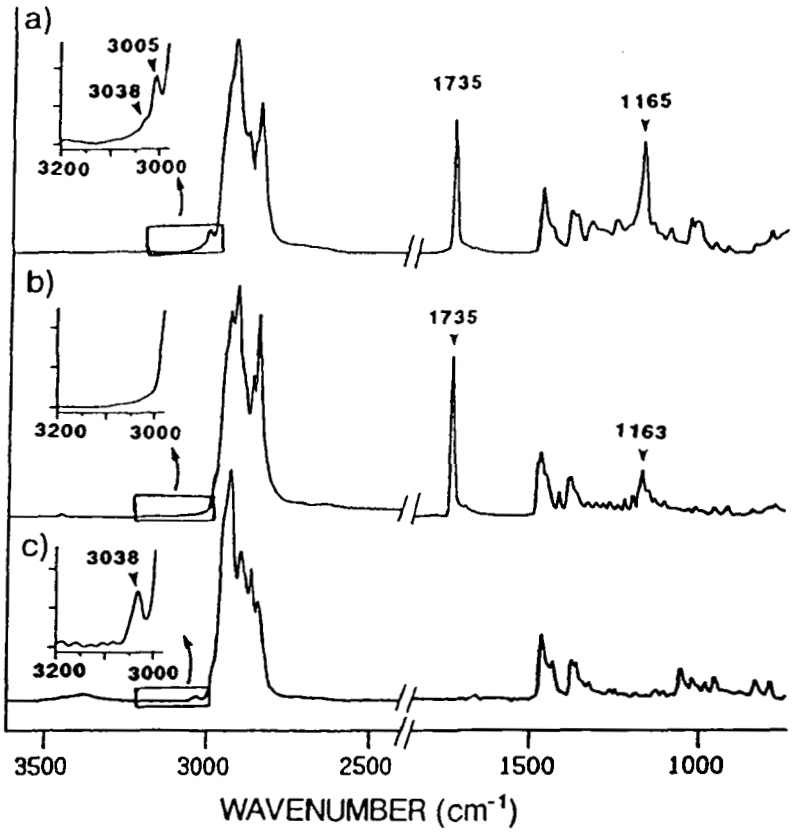

Figure 11. Fourier transform infrared spectra of reference compounds (a) cholesteryl oleate, (b) cholestanol palmitate, and (c) cholesterol. Used by permission, [84].

using a 24- x 24-μm aperture; for example, the lipid content of the brain was mapped in one study [87].

The twitcher mouse exhibits an enzyme deficiency similar to that observed in humans who have globoid cell leukodystrophy (or Krabbe's disease). The enzyme deficiency allows psychosine (galactosylsphigosine) to accumulate and adversely affect myelination in the brain. FT-IR microspectroscopy was used to

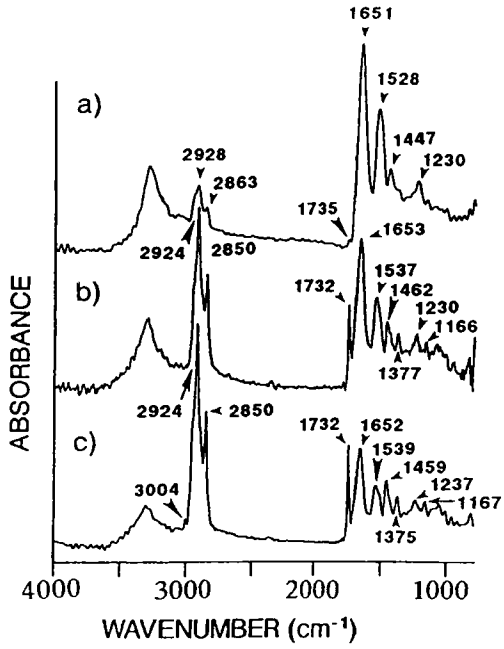

Figure 12. Infrared spectra of 20- x 20-μm regions of 5-μm thick section of artery from the (a) media between 160 and 180 μm from the edge of the media, (b) intima between 340 and 360 μm, and (c) intima region between 380 and 400 μm. Used by permission, [84].

determine if excess psychosine could be detected in the hindbrain and cerebrum in the twitcher mouse, and the spectroscopic results were compared to more conventional histopathologic methods [89, 90]. The only spectroscopic evidence found was in the region of the CH_2 antisymmetric stretch near 2920 cm^{-1}. Brain tissue from normal mice exhibited a band between 2925 and 2924 cm^{-1}, and the corresponding psychosine band is located at 2920 cm^{-1}. The broadening of this band in twitcher mouse brains and its shift to lower frequencies (lower than 2924 cm^{-1}) was ascribed to overlap of brain tissue and excess psychosine. These data are summarized in Figure 17.

By comparison, shiverer mice have a mutation in the myelin basic protein (MBP) gene which inhibits the normal process of myelin deposition [89]. Unlike

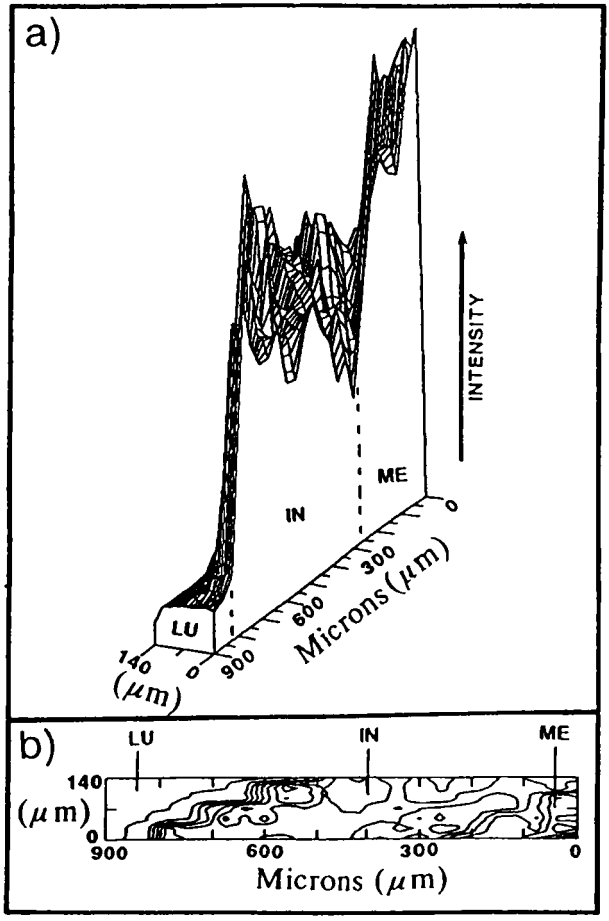

Figure 13. Plots of the amide I infrared absorbance band of 20- x 20-μm segments of an artery showing (a) an axonometric plot across the artery from the lumen (LU) through the intima (IN) to the media (ME) and (b) a contour map of the same region of artery. Used by permission, [84].

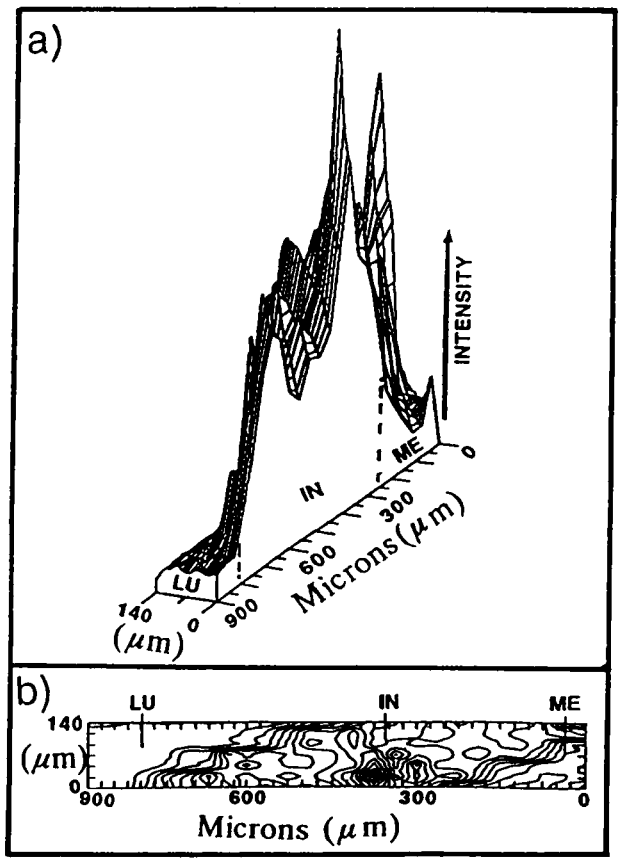

Figure 14. Plots of the ester C=O infrared absorbance band of 20- x 20-μm segments of an artery showing (a) an axonometric plot across the artery from the lumen (LU) through the intima (IN) to the media (ME) and (b) a contour map of the same region of artery. Used by permission, [84].

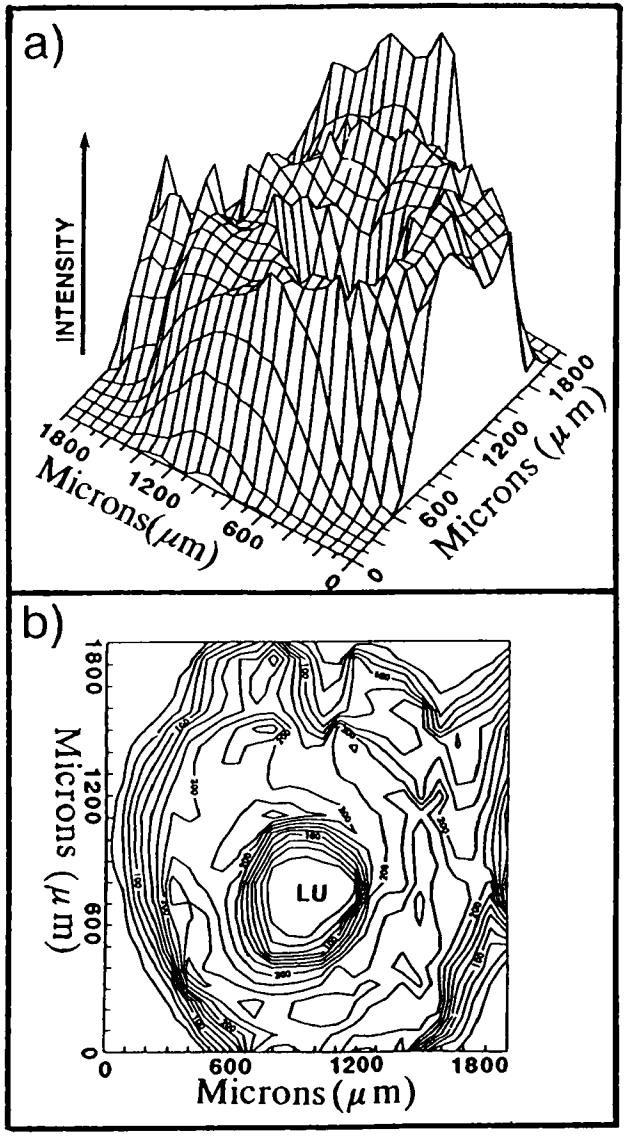

Figure 15. Plots of the amide I infrared absorbance band of a cross-section of an artery: (a) axonometric plot and (b) contour plot. Used by permission, [84].

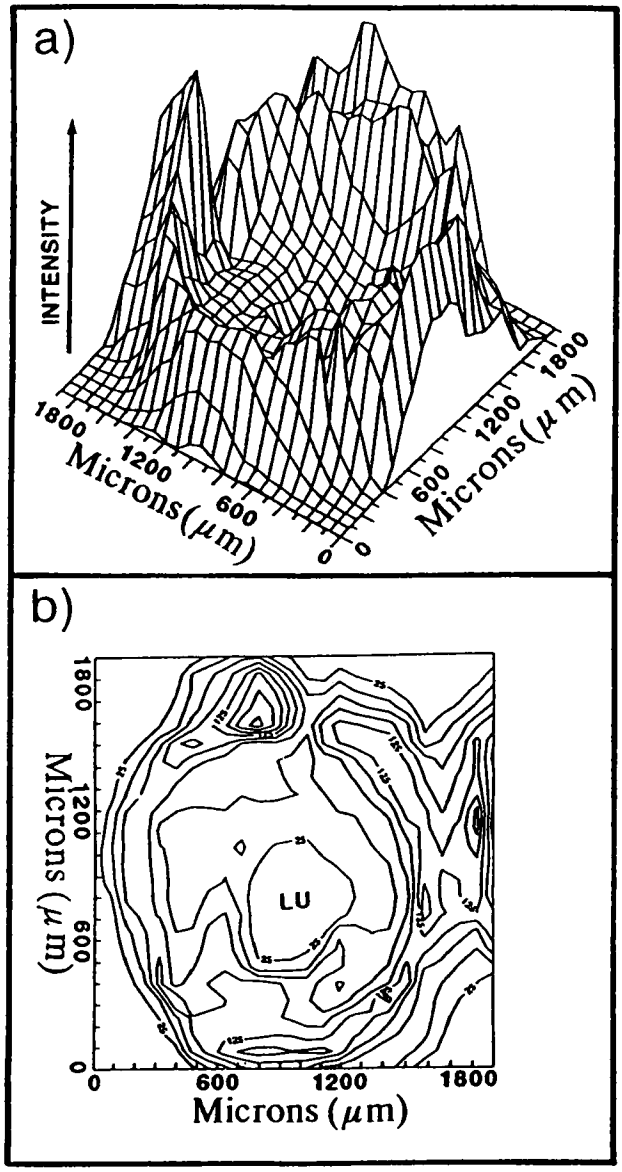

Figure 16. Plots of the ester C=O infrared absorbance band of a cross-section of an artery: (a) axonometric plot and (b) contour plot. Used by permission, [84].

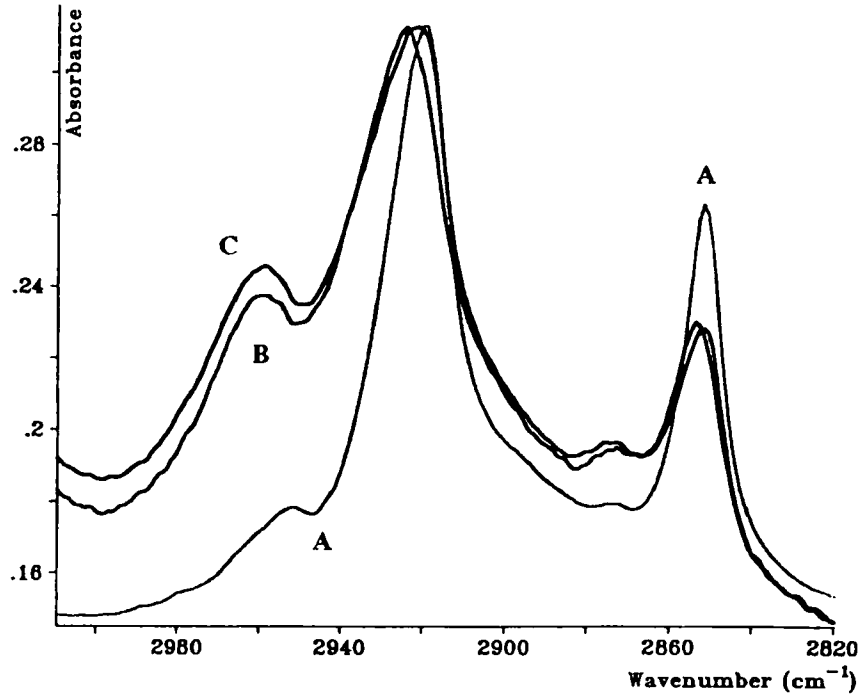

Figure 17. Infrared spectra of the 3010-2820-cm^{-1} region from (A) psychosine, (B) hindbrain white matter from a twitcher mouse, and (C) hindbrain white matter from a normal mouse. Used by permission, [90].

the situation for normal mice, FT-IR spectra of white matter and gray matter of shiverer mice showed very few differences. A detailed interpretation for the shiverer mouse was not possible, but the sensitivity of FT-IR spectra to the chemical structures of abnormal brains was clearly demonstrated.

In another study, spectral changes in bands associated with lipids and proteins were monitored in response to the introduction of blood into the white matter of the brain [91]. Bands at 3015, 2927, 1740, 1469, 1235, and 1085 cm^{-1} were observed to decrease relative to the amide II band at approximately 1550 cm^{-1} as a result of the physiologic reaction to extravasated blood in the brain. There was also a slight shift to lower wavenumber for the amide II band. These results

suggest that lipid peroxidation is involved with the pathology in the vicinity of the site where the blood was introduced.

E. Calculi and Crystalline Materials

Crystalline materials form in various organs of the body. The ultimate outcome can range from the deposition of small crystals in tissue to the formation of calculi (stones) as large as a few centimeters in size. For the latter, wet chemical methods and macroscopic spectroscopy techniques can be used to identify the constitutents, but for layered calculi and small crystals, microspectroscopy is more useful.

Kidney stones have received considerable attention. Dispersive and FT-Raman techniques with laser spots focused to less than 1 mm in diameter in conventional (macroscopic) sampling configurations have been used to characterize nearly pure stones composed of cystine [92, 93], uric acid [93, 94], calcium oxalate [93, 95], and calcium phosphates [96]. Stones composed of proteins and other organics and those composed of inorganic mixtures have also been studied [97, 98]. Visible excitation frequently resulted in significant fluorescence from the specimens, but near-infrared excitation (FT-Raman) eliminated this problem.

Calculi have also been investigated using a Raman microprobe spectrometer [99]. Segments of calculi as small as 2 μm were analyzed directly in the Raman instrument and as KBr pellets in an infrared spectrometer. The detailed study of the components of calculi can be useful in understanding the etiology of the formation of the stones.

These authors identified more than sixty organic and inorganic components of urinary calculi [99]. Both forms of calcium oxalate (monohydrate and dihydrate) were distinguished by their characteristic Raman spectra. Calcite (a form of calcium carbonate), calcium phosphates, and magnesium phosphates were among the inorganic species found in many of the calculi studied.

The carbonate apatites exhibited a set of distinct infrared bands, but the Raman spectra showed a shift in the phosphate P-O stretch from 959 cm^{-1} for apatite to 963 cm^{-1} for the saturated carbonate apatite [99]. A similar shift was also observed for apatites in atherosclerotic plaques [81].

Magnesium hydrogen phosphate trihydrate (newberyite) was found on the outer layers of calculi containing ammonium magnesium phosphate hexahydrate (struvite) and in struvite stones or specimens which had been left in air for extended periods of time. The data suggest that this relatively facile transformation accounts for the newberyite found in urinary calculi [99].

A number of organic materials were also identified by their infrared and Raman spectra. Various urate salts and the anhydrous and dihydrate forms of uric acid were found in many calculi. The tendency of uric acid dihydrate to decompose under laser irradaition in the Raman microprobe emphasizes the need for infrared data as a complement to the Raman spectra.

The purine derivatives xanthine, hypoxanthine, and 2,8-dihydroxyadenine were also observed in the Raman spectra despite significant fluorescence. Infrared spectra, when available, were sufficient to provide positive identification, but the differences in spatial resolution suggest that both types of spectra be collected. Xanthine was found in a patient suffering from congenital xanthinuria, and the spectroscopic data confirmed the diagnosis. Similarly, patients with cystinuria form calculi composed of another organic component, cystine, which was identified by its characteristic infrared and Raman spectra. The latter spectrum is particularly useful because of a very intense line near 500 cm-1 which is due to the S-S stretching vibration [99].

A fiber optics probe with near-infrared excitation was used in one study to demonstrate the feasibility of conducting *in vivo* determinations of the composition of calculi. Information of this type could potentially be used in treating patients without resorting to surgery [100].

In patients suffering from oxalosis, calcium oxalate has been identified in kidney tissue biopsies by FT-IR microspectroscopy [101]. As indicated in Figure 18, crystalline calcium oxalate is also frequently found in urine samples.

Limited animal studies in which the factors affecting the disposition of calculus materials in the kidney have been conducted. The formation of calcite ($CaCO_3$), calcium oxalate, and hydroxyapatite was confirmed in rabbit kidney tubules using a Raman microprobe [102]. Similarly, the kidneys of eels were found to contain calcium oxalate and calcium phosphates [103].

Macroscopic Raman studies of cholesterol- and bilirubin-containing gallstones have been reported [104]. More recently, Raman microprobe data and FT-IR spectra using a beam condenser and apertures between 50 and 200 μm have been applied [105]. FT-IR spectra were used to identify cholesterol as the only

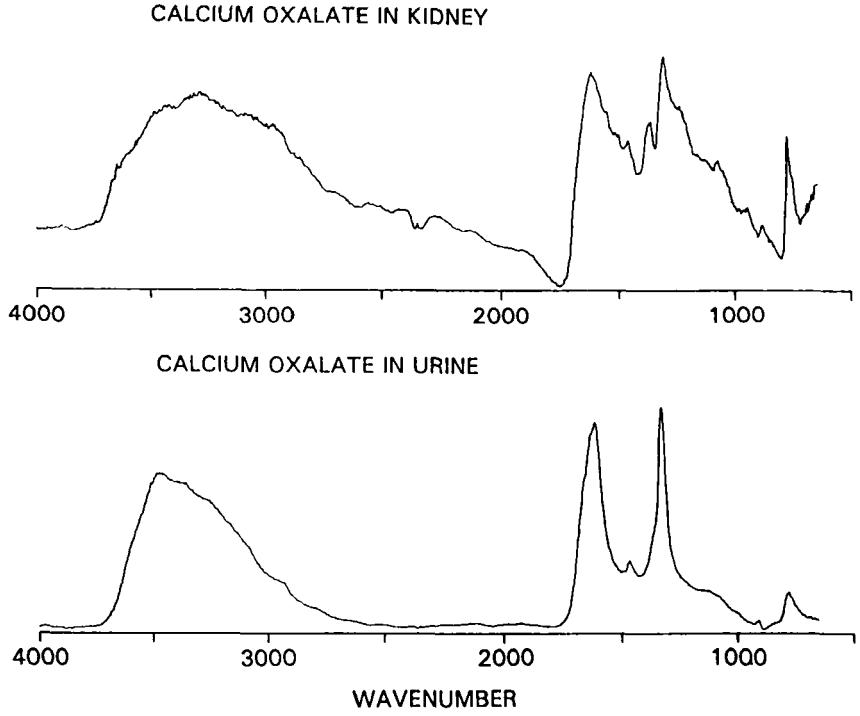

Figure 18. Infrared spectra of calcium oxalate in kidney tissue and isolated from urine.

component of one gallstone. In a bilirubin gallstone, two different forms of bilirubin (an acid form and a calcium salt) were identified by their characteristic resonance Raman spectra. A layered gallstone was found to have a yellowish-brown outer layer of cholesterol, a brown center composed of bilirubin (acid and salt forms), and a middle layer consisting of $Ca_3(PO_4)_2$, cholesterol, and bilirubin (both forms). This stone and a bilirubin stone were also found to have white particles 20 to 100 μm in size identified as a calcium salt of a fatty acid interspersed in the more darkly colored regions [105].

Deposition of calcium pyrophosphate in various tissue specimens has been studied by using infrared and Raman spectroscopy. Infrared spectra of particles removed from knee joint synovial tissue and soft tissue near the metatarsal joint

were used to confirm a presumptive diagnosis of calcium pyrophosphate based on polarized light microscopy, scanning electron microscopy, and energy dispersive X-ray analysis [106]. Similarly, pelvic deposits were identified as calcium pyrophosphate from the intense Raman line at 1050 cm^{-1} [107]. Raman microspectroscopy data were used to confirm calcium pyrophosphate in synovial fluid, synovial tissue, and cartilage and to identify sodium urate in synovial fluid and a gout-related tophus [108].

Cystinosis is another disease in which crystalline material can be deposited in tissue. Infrared and Raman microspectra of cystine in liver and spleen tissue were reported [109]. The Raman spectrum exhibited the strong S-S vibration near 500 cm^{-1} (see Figure 19) which is characteristic of the disulfide linkage and also observed in cystine-containing calculi [92, 99]. The infrared spectrum of cystine in Figure 20 also matches those of crystals in the liver and spleen tissue.

Mendelsohn *et al.* used infrared microspectroscopy to study mineralization in the femurs of normal and rachitic (vitamin-D deficient) rats [110]. By comparing the intensities of the phosphate vibrations of the inorganic materials with the intensities of the amide-I and amide-II vibrations due to protein (primarily collagen), they were able to show the extent of mineralization as a function of position along the bone in approximately 20 μm steps. The two groups of rats exhibited different rates of ossification, and the amount of mineralized bone in the rachitic rats was found to be approximately 60% of the value found for normal rats.

F. Foreign Materials

Foreign materials in tissue constitute a large area of application of microspectroscopy. Environmental intake, the administration of therapeutic drugs, and surgical procedures account for many foreign materials in a patient, and the body's reaction to these materials can be described histopathologically.

Pieces of polymeric materials used in surgical procedures are often large enough to be viewed in an FT-IR microscope [111]. Poly(tetrafluoroethylene) from a heart graft and nylon from ocular valve implants were readily identified. As an example, Figure 21 shows spectra of tissue (protein), nylon in tissue, and a reference material. FT-IR and Raman microspectroscopy have been used to confirm the presence of silicone polymers in skin biopsies [111] and an axillary

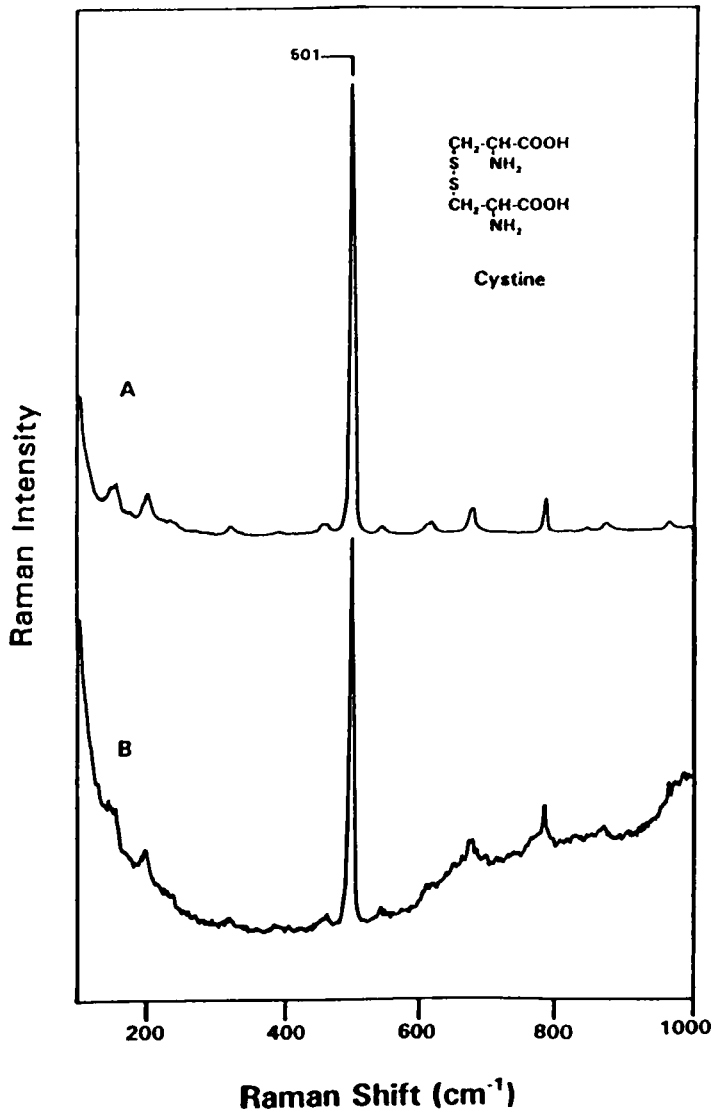

Figure 19. Raman spectra of (A) authentic L-cystine crystal and (B) cystine in liver tissue using a 5-μm laser spot. Used by permission, [109].

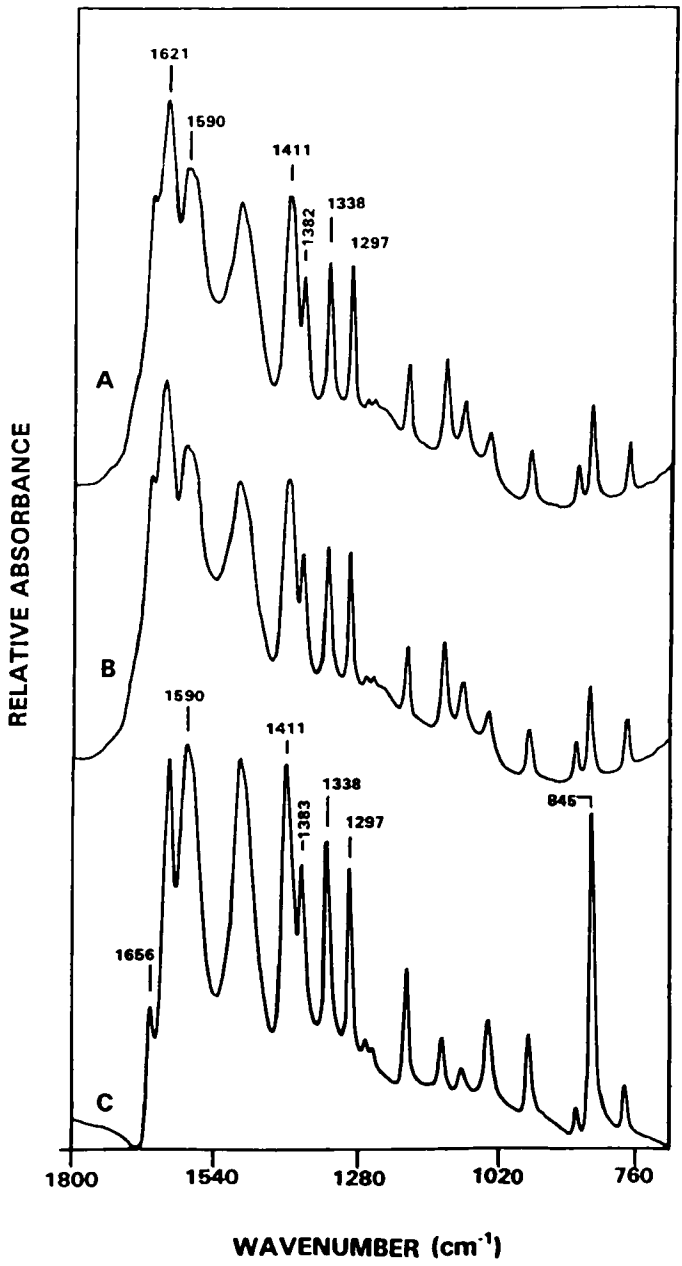

Figure 20. Infrared spectra of cystine crystals in (A) liver tissue and (B) spleen tissue and (C) authentic L-cystine specimen using a 30-μm circular aperture. Used by permission, [109].

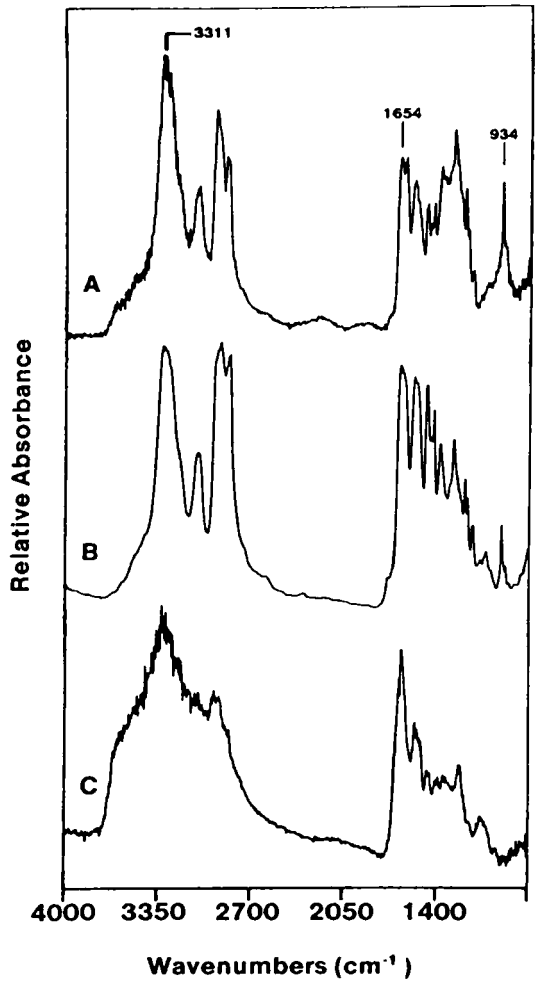

Figure 21. Infrared spectra of (A) nylon and surrounding protein, (B) nylon 6/6 reference material, and (C) protein from a region of tissue away from the nylon. Used by permission, [111].

lymph node of a patient with a finger joint prosthesis (see Figure 22) [27], respectively. Polyethylene, polyurethane, and polysulfone from orthopedic prostheses were studied using FT-IR microspectroscopy [111], and Figure 23 is representative of the data obtained. Other polymers which have been located in bone biopsy tissue after reconstructive surgery include poly(glycolic acid) and polydioxanon [101]. Screws made of poly(glycolic acid) are commonly used instead of metal screws or pins to aid the healing of broken bones, and the material is slowly metabolized as the bone heals. In some cases, however, pieces of poly(glycolic acid) can induce a foreign-body reaction.

Plastics and other materials also find their way into the lungs. Small pieces of poly(methyl methacrylate) and polyethylene were identified by FT-IR microspectroscopy in lung lavage material taken from a patient who was exposed to a highly particle-laden atmosphere in an occupational setting [101]. In a recent report [112], a polystyrene sulfonate material was found in lung tissue using polarized light microscopy and FT-IR microspectroscopy (see Figure 24. A preparation of the material, taken orally, acts as an ion exchange resin in the treatment of hyperkalemia. Its presence in the lung was probably the result of aspiration of the resin after regurgitation. In another case, fragments of a cephalosporin derivative, which had been prescribed for a patient, were located in the patient's kidney and subsequently identified by using an infrared microscope [101].

Greve and coworkers utilized a Raman microprobe in studying smaller particles. Spectra in Figures 25 and 26 indicate the presence of calcite ($CaCO_3$) and magnesite ($MgCO_3$) in lung tissue as a result of inhalation [113, 114]. Similarly, quartz, talc, and rutile (TiO_2) were found in lymph nodes (See Figure 27) [113] presumably transported there by macrophages.

Breast prostheses, used for reconstruction or augmentation, have received considerable attention, especially since the FDA's 1992 ban on the use of silicone (polysiloxane) gel-filled implants [115]. Saline-filled implants, with shells constructed of silicone elastomer, were still available at the time of this writing, but their continued use was under review. Gel-filled implants were known to leak small quantities of silicone gel into the surrounding tissue, and of course, significant amounts of gel would be in contact with breast tissue if an implant were to rupture.

The most commonly used silicone for breast prostheses is polydimethylsiloxane (PDMS) whose consistency can vary from oil to gel to

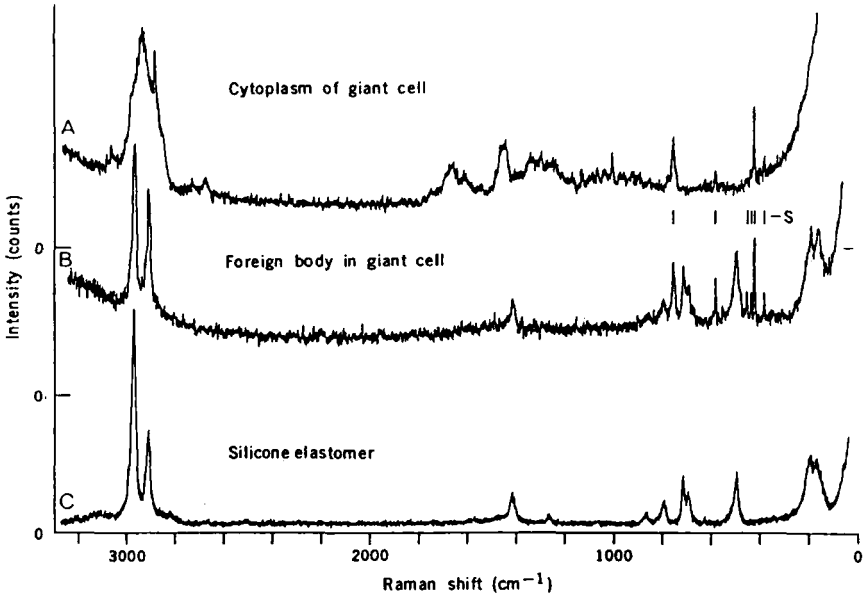

Figure 22. Raman spectra of (A) lymph node tissue, (B) foreign material in the lymph node, (C) silicone elastomer. (The lines marked with "S" in spectra (A) and (B) are due to the sapphire substrate. Used by permission, [27].

elastomer depending on parameters such as chain length and degree of crosslinking. One of the human body's reactions to this material is the formation of fibrous tissue around the implant, and the precise nature of this fibrous "capsule" depends upon the prosthetic device and the patient's immune system.

Prior to the development of implants with a silicone elastomer shell, materials like silicone, paraffin, and others were injected directly into breast tissue as an augmentation procedure. Infrared spectroscopy has been used for many years to identify silicone from injections of this sort [116], from breast implants [117-119], and from dialysis therapy [120]. Kossovsky *et al.* recently used attenuated total reflection (ATR) FT-IR [121] to identify silicone, mineral oil, and soy or olive oil in breast tissue from patients who underwent injection therapy. It is important to note that sample preparation is important in cases such as these so

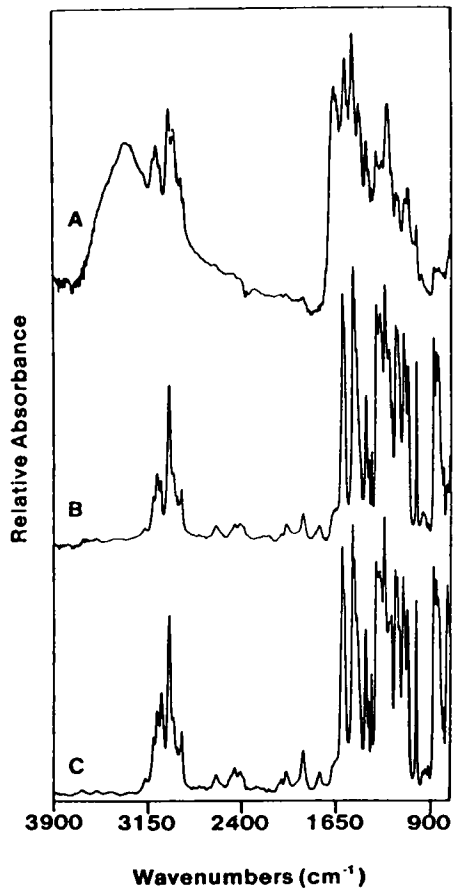

Figure 23. Infrared spectra of (A) polysulfone and surrounding tissue (no aperture), (B) polysulfone in tissue (30-μm aperture), and (C) polysulfone reference material. Used by permission, [111].

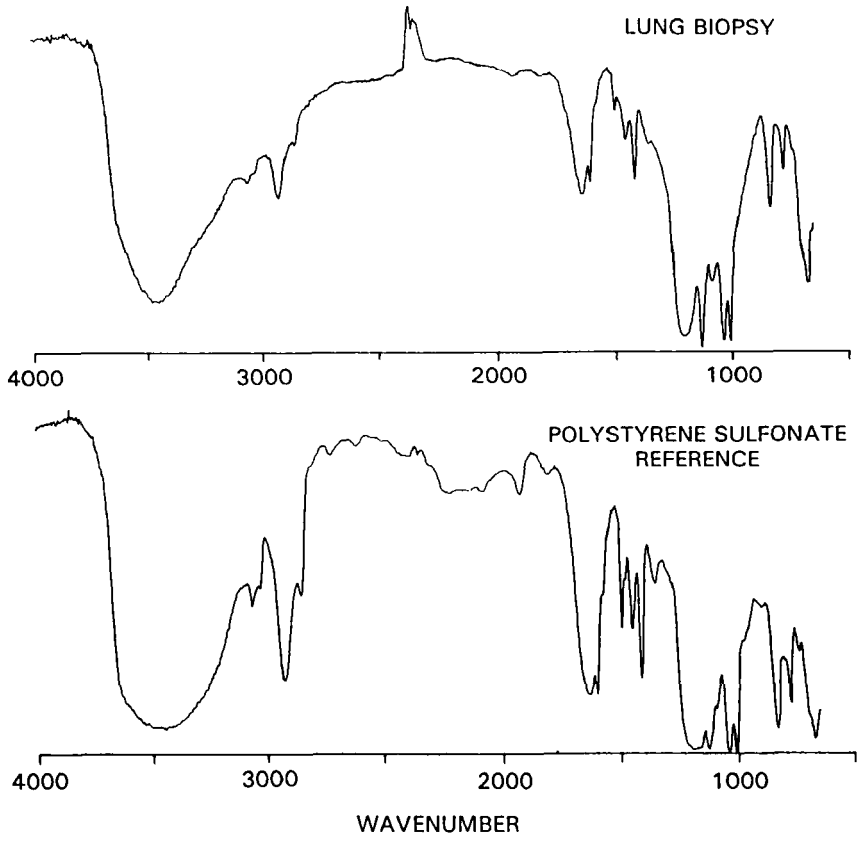

Figure 24. Infrared spectra of foreign material in lung biopsy tissue and polystyrene sulfonate reference material.

that the hydrophobic foreign materials are not lost during conventional tissue processing with organic solvents.

More recently, FT-IR and Raman microscopy techniques have been applied to the analysis of tissue sections from breast implant patients [122-125]. Silicone gel has been found as isolated accumulations as large as 50 μm or intermingled with tissue protein (in capsular tissue and lymph nodes). The presence of silicone gel or elastomer can be confirmed with the relatively distinct bands in either the

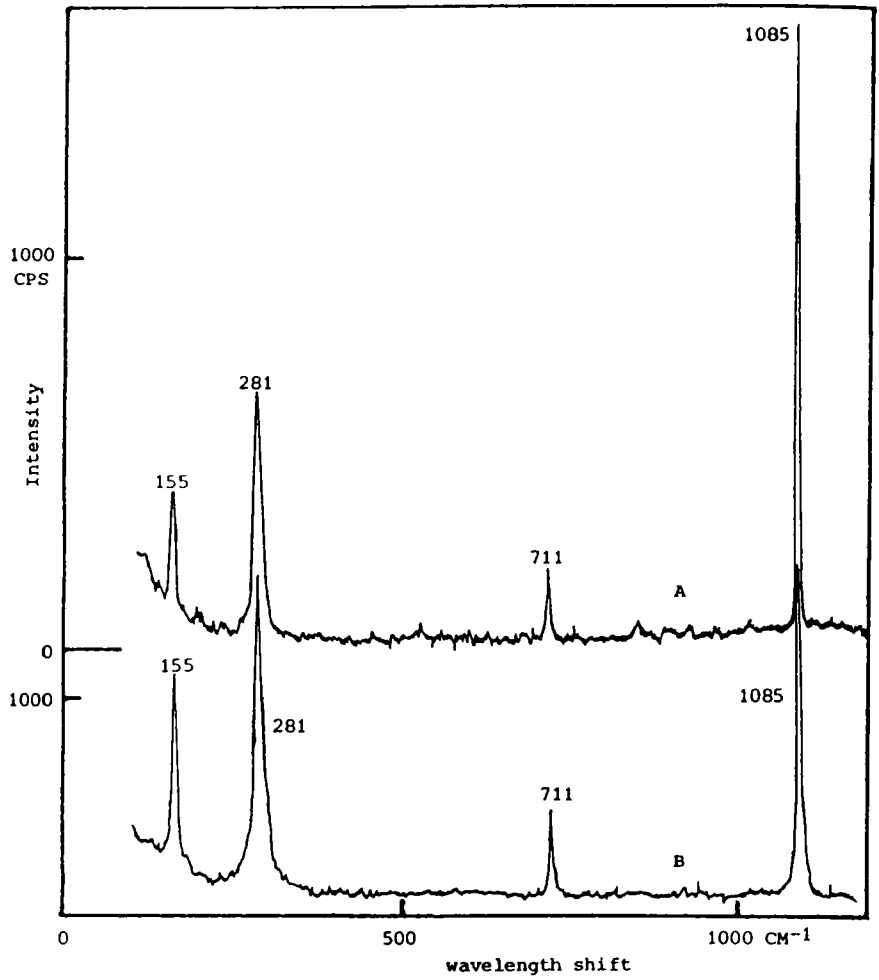

Figure 25. Raman spectra of (A) an inclusion in lung tissue and (B) calcite ($CaCO_3$) reference material. Used by permission, [114].

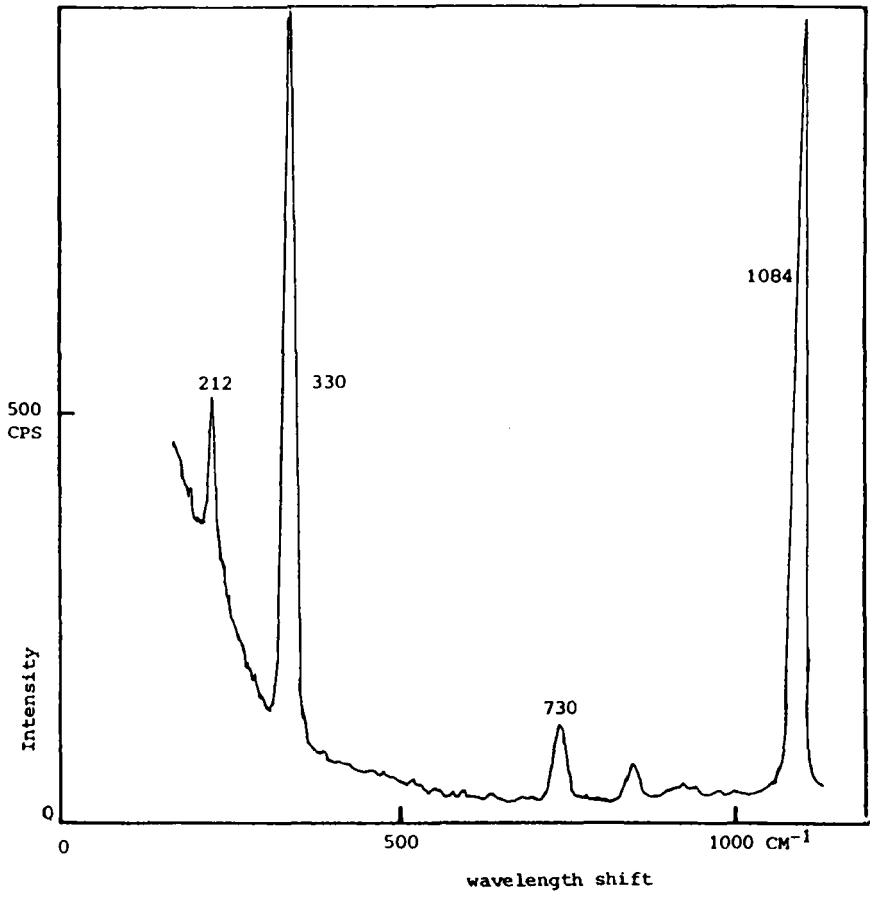

Figure 26. Raman spectrum of an inclusion in lung tissue shown to be magnesite ($MgCO_3$). Used by permission, [114].

infrared or Raman spectra. Infrared spectra such as those in Figure 28 show the characteristic bands of the PDMS which can be isolated or overlapped by protein. These bands can also be used to visualize the presence of silicone in a spectral map (See Figure 29).

Raman spectra of silicone in breast tissue have been recorded using 514.5-nm excitation with a Raman microscope (2-μm spatial resolution) [124] and in

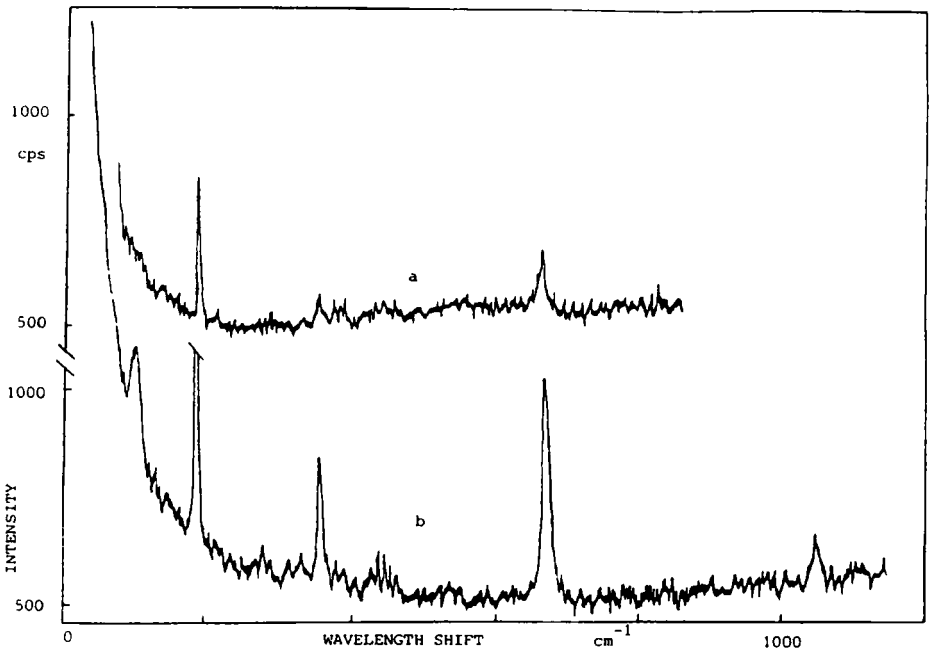

Figure 27. Raman spectra of (a) an inclusion in lymph-node tissue and (b) talc reference material. Used by permission, [113].

lymph node tissue using 782-nm excitation with a laser spot focused to 200 μm [126]. In the latter study it was suggested that a fiber-optics probe could be utilized for *in vivo* Raman diagnoses of silicone lymphadenopathy.

The manufacture of breast implants had involved other polymers as well. Polyurethane coverings for the sliicon elastomer were used for a short time to limit the formation of the fibrous capsule surrounding an implant, and Dacron patches were added to some implants to assist in affixing the implants to the patients' chest muscle. These materials were evident in FT-IR and Raman spectra of sections of breast capsular tissue [123-125].

G. Ophthalmic Applications

Cai *et al.* [127] used a 50-μm laser spot and an optical mask in a conventional Raman spectrometer while Vrensen and coworkers [128-130]

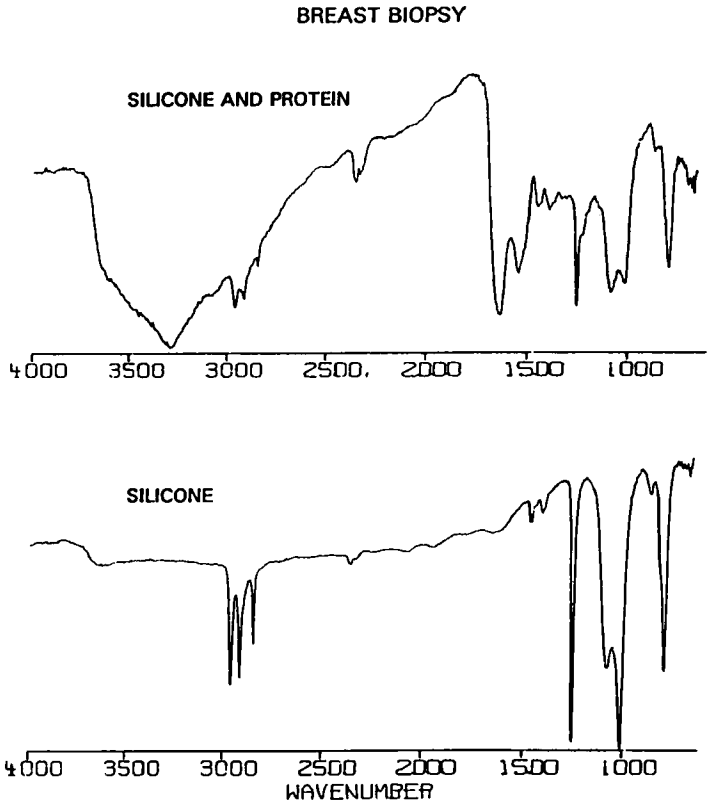

Figure 28. FT-IR spectra of breast biopsy tissue showing regions containing silicone and protein (upper trace) and isolated silicone (lower trace).

utilized a Raman microprobe (2-μm spatial resolution) to determine water content in eye lenses in humans and animals. The basis of these analyses is a comparison of intensities of Raman lines attributable to protein and water; intensity ratios are then converted to weight percentages. Cai *et al.* [127] used whole lenses from rats and recorded spectra along an equatorial diameter of the lens. They concluded that the water content in the central nucleus of a normal lens is nearly constant at approximately 50% and increases to approximately 80% in the cortex (edge). A galactose-induced cataract had a water percentage of more than 70% in the nucleus and over 90% in the cortex. The sulfhydryl bands were also compared to the

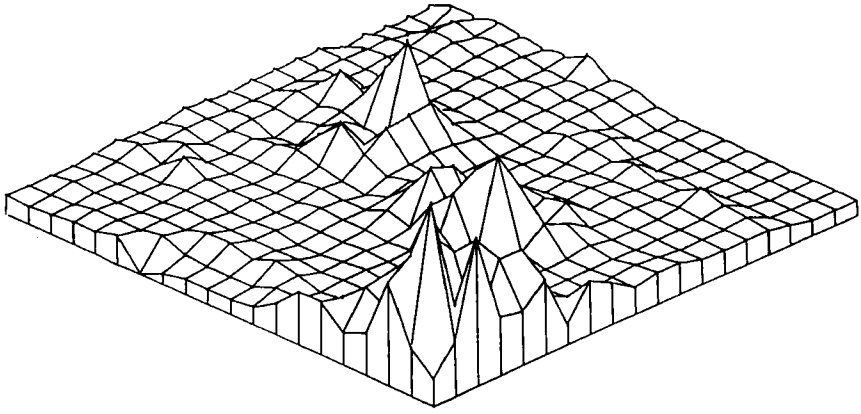

Figure 29. Infrared map of a tissue section highlighting absorption bands attributed to silicone gel.

protein bands, but the variation in intensities were not completely understood nor were they interpreted as evidence of the formation of disulfide linkages in the cataract [127].

With the microprobe, Siebinga *et al.* [130] mapped the water percentage in slices taken from human lenses. The relatively constant value of approximately 65% water in the nucleus extended to within 0.05 to 0.2 mm of the edge of the lens. This steep gradient in the human lens [130] was contrasted to the more gradual variation reported for rabbits [129]. The amount of water was observed to be larger for older patients, and it was suggested that the water:protein ratio affects the refractive index of the lens and, thereby, the vision of the patient.

"Christmas tree" cataracts are characterized by the presence of refractile, multi-colored needle-shaped inclusions located in an otherwise clear lens. Various suggestions regarding the origins and composition of the inclusions have been offered, but the lack of convincing evidence prompted a study involving transmission electron microscopy, scanning electron microscopy coupled with energy dispersive X-ray analysis (EDXA), and a confocal Raman microspectrometer using excitation at 660 nm [131]. The EDXA results showed sulfur and calcium at higher levels than in normal lens tissue, but no increase was

observed for phosphorus; the precise interpretation of these findings is not clear and requires more work.

Raman lines in three regions of the spectra exhibited increased relative intensity, and these were interpreted as arising from S-S and C-S vibrations. The authors concluded that crystals of compounds like cystine constitute the refractile material and are responsible for the observed data [131]. They also suggested that these materials are the products of enzymatic protein breakdown, but additional work will be required to confirm these hypotheses.

H. Hair Analysis

One final example in which microspectroscopy can provide data not otherwise available is in the analysis of drugs in hair [132, 133]. Traditional bulk analysis involves extraction of the drugs from hair and quantitation by gas chromatography or GC/MS. Microsampling has been used to determine whether drugs were located on the surface of the hair, in the cortex, or in the central medulla. Figure 30 shows the result of a map of a transverse cross-section which shows that hydromorphone concentrates in the protein of the medulla of the hair. Figure 31 provides another representation of these data. The coincidence of the drug with the interior of the hair leaves no doubt that the drug was ingested and subsequently incorporated into the hair as it grew. Not all drugs interact with the medulla in the same way, and additional work to determine the limits of this technique is underway.

IV. FUTURE PROSPECTS

The future of vibrational microscopy is as exciting now as it was when the concept was originally put into practice. New applications are identified regularly, and there seems to be no limit on the applications to medicine, biochemistry, and toxicology. The key to the future is to configure microspectrometers to provide readily interpretable data which complement the more established tools of microscopy.

In the mid-infrared region, an important improvement in signal levels with small apertures (as small as 6 μm) has been achieved by using synchrotrons as

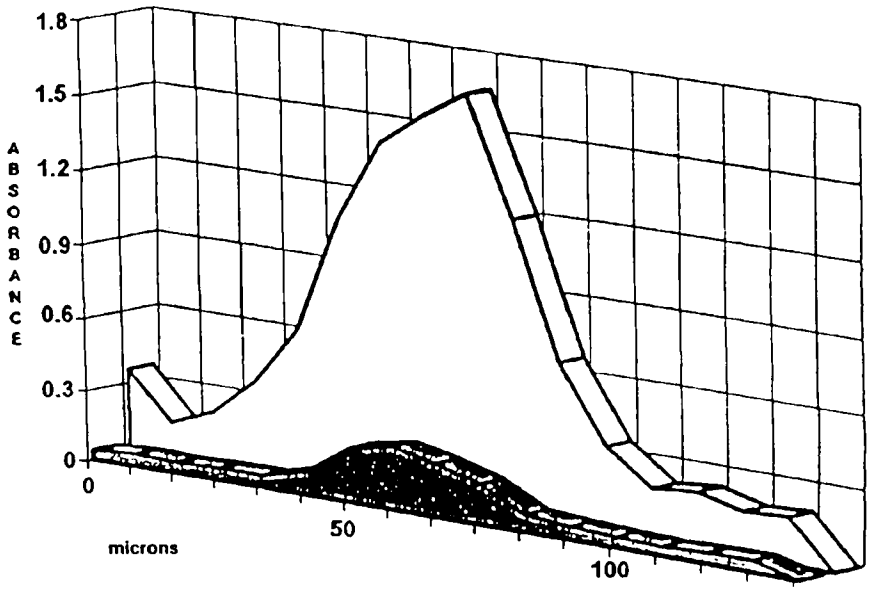

Figure 30. Infrared spectral map along the diameter of a cross-section of hair containing hydromorphone. The light-colored portion was mapped for protein; the dark portion represents the drug. Used by permission, [132].

sources of infrared radiation [45]. The total output energy is not significantly different from that available from a more conventional blackbody infrared source, but the synchrotron radiation is concentrated into a relatively small beam which is well-suited for an FT-IR spectrometer. Brookhaven National Laboratory, the National Institute for Science and Technology (NIST), and other facilities are exploring the possibilities for making access to their synchrotron sources available to visiting researchers.

With dedicated computers and sophisticated software, near infrared spectroscopy has been used in many macroscopic applications involving quantitative analysis of complex mixtures [134]. There are also examples of near infrared studies of biomolecules and tumors in which bulk specimens were used to demonstrate the utility of near infrared data for diagnoses [135, 136]. Recently, the near-infrared region has been used for imaging purposes because detection is

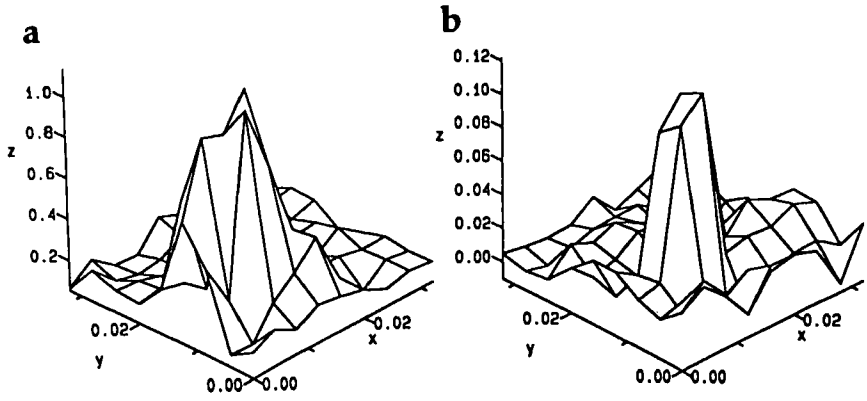

Figure 31. Infrared spectral map of hair showing the relative amounts of (a) protein and (b) drug. Used by permission, [132].

relatively easy and standard microscope optics are compatible with near infrared radiation [59, 60]. Scanning monochromators can be used for wavelength selection, but much of the imaging was accomplished with faster acousto-optic tunable filter (AOTF) or liquid crystal modulators.

Raman imaging using long-wavelength excitation can be done with the same near infrared spectrometers, but commercially available imaging instruments are configured with visible lasers. The choice of excitation wavelength for Raman imaging depends on the same parameters discussed earlier wherein it is necessary to weigh the effects of laser power, scattering efficiencies, resonance enhancements, interfering fluorescence, and other factors. One significant advantage of Raman imaging relative to point-by-point Raman mapping is that the power density of the laser on the specimen is greatly reduced because a large area is illuminated at any given time. Fluorescence problems are usually minimized by using laser radiation in the 600- to 700-nm range [137-139].

There is also promise for imaging in the mid-infrared region [140]. Sensitive detectors of suitable size are currently available, and commercial FT-IR imaging spectrometers are expected before too long.

While imaging represents the next significant step for all applications of infrared and Raman microspectroscopy, vibrational microscopy will continue to be

used for the identification of individual materials in tissue simply because other methods cannot provide comparably definitive information. As more studies are conducted, there will be a better understanding of the molecular processes involved in biomolecular interactions. Cellular functions and metabolic processes constitute areas where considerable work needs to be completed using vibrational microscopy.

Except in isolated applications, the automated mapping systems in use today will give way to powerful imaging spectrometer systems because of the wealth of information which can be collected rapidly. The analysis of vibrational images offers a challenge as one tries to compare them with information from conventional light microscopes. Vibrational data can be viewed in the same way as specialized histochemical stains which are designed to highlight particular cellular features under a light microscope. Infrared and Raman images offer the added advantage that the images can be changed as different vibrational markers are selected.

Image sizes are limited by detector size and, to some extent, data storage capacity, but improvements in these areas are surely guaranteed by the semiconductor industry. Three-dimensional images constructed from vibrational data obtained on confocal microscopes and other depth profiling procedures will allow large segments of tissue to be studied. Vibrational imaging can be integrated into medical diagnosis by taking advantage of the existing technology in use with other imaging modes. With the variety of problems in medical research and diagnosis there is an increasing need for the information available from infrared and Raman microspectroscopy.

REFERENCES

1. Cramers, CA; Leclercq, PA. *Crit Rev Anal Chem* **1988**, *20*, 117-147.
2. Brown, PR. High-performance liquid chromatography: Past developments, present status, and future trends. *Anal Chem* **1990**, *62*, 995A-1008A.
3. Albin, M; Grossman, PD; Moring, SE. Sensitivity enhancement for capillary electrophoresis. *Anal Chem* **1993**, *65*, 489A-497A.
4. Wishnok, JS. Environmental carcinogens: *in vivo* monitoring using GC/MS. *Anal Chem* **1992**, *64*, 1126A-1135A. [MS ref]
5. Smith, AL. *Applied Infrared Spectroscopy: Fundamentals, Techniques, and Analytical Problem-Solving*. Wiley, New York, 1979.

6. Griffiths, PR; deHaseth, JA. *Fourier Transform Infrared Spectrometry*, Wiley, New York, 1986.
7. Grasselli, JG; Snavely, MK; Bulkin, BJ. *Chemical applications of Raman spectroscopy*, Wiley, New York, 1981.
8. Grasselli, JG; Bulkin, BJ, ed. *Analytical Raman Spectroscopy*, Wiley, New York, 1991.
9. Clark, RJH; Hester, RE; eds. *Advances in Infrared and Raman Spectroscopy, Spectroscopy of Biological Systems*, Wiley-Heyden, New York, 1986.
10. Schmid, ED; Schneider, FW; Siebert, F. *Spectroscopy of Biological Molecules: New Advances*. Wiley, New York, 1988.
11. Ozaki, Y. Medical application of Raman spectroscopy. *Appl Spectrosc Rev* **1988**, *24*, 259-312.
12. Fabian, H; Anzenbacher, P. New developments in Raman spectroscopy of biological systems. *Vib Spectrosc* **1993**, *4*, 125-148.
13. Thomas, GJ Jr; Benevides, JM; Prescott, B. DNA and RNA structures in crystals, fibers, and solutions by Raman spectroscopy with applications to nucleoproteins. in *Biomolecular Stereodynamics IV*. Sarma, RH; Sarma, MH; eds. Adenine Press, New York, pp. 227-253.
14. Levin, IW. *Advances in Infrared and Raman Spectroscopy*; Clark, RJH; Hester, RE; eds. Wiley-Heyden, New York, 1984; Vol 11, Chapter 1.
15. Barer, R; Cole, ARH; Thompson, HW. Infra-red spectroscopy with the reflecting microscope in physics, chemistry, and biology. *Nature* **1949**, *163*, 198-201.
16. Coates, VJ; Offner, A; Siegler, EH. Design and performance of an infrared-microscope attachment. *J Opt Soc* **1953**, *47*, 984-989.
17. Messerschmidt, RG. in *Infrared Microspectroscopy: Theory and Applications*. Messerschmidt, RG; Harthcock, MA; eds. Marcel Dekker, New York, 1988, Chapter 1, pp. 1-19.
18. Sommer, AJ; Katon, JE. Diffraction-induced stray light in infrared microspectroscopy and its effect on spatial resolution. *Appl Spectrosc* **1991**, *45*, 1633-1640.
19. Delhaye, M; Dhamelincourt, P. Raman microprobe with laser excitation. *J Raman Spectrosc* **1975**, *3*, 33.
20. Dhamelincourt, P; Wallart, F; Leclercq, M; N'Guyen, AT; Landon, DO. Laser Raman molecular microprobe (MOLE). *Anal Chem* **1979**, *51*, 414A-421A.
21. Anderson, ME; Muggli, RZ. Microscopical techniques with the molecular optics laser examiner Raman microprobe. *Anal Chem* **1981**, *53*, 1772-1777.
22. Adar, F. Developments of the Raman microprobe - instrumentation and applications. *Microchem J* **1988**, *38*, 50-79.

23. Rosasco, GJ; Etz, ES; Cassatt, WA. The analysis of discrete fine particles by Raman spectroscopy. *Appl Spectrosc* **1975**, *29*, 396-404.
24. Rosasco, GJ; Roedder, E; Simmons, JH. Laser-excited Raman spectroscopy for nondestructive partial analysis of individual phases in fluid inclusions in minerals. *Science* **1975**, *190*, 557-560.
25. Blaha, JJ; Rosasco, GJ. Raman microprobe spectra of individual microcrystals and fibers of talc, tremolite, and related silicate minerals. *Anal Chem* **1978**, *50*, 892-896.
26. Etz, ES. Raman microprobe analysis: principles and applications. *Scanning Electron Microsc* **1979**, *1*, 67-92.
27. Abraham, JL; Etz, ES. Molecular microanalysis of pathological specimens *in situ* with a laser-Raman microprobe. *Science* **1979**, *206*, 716-718.
28. Rosasco, GT. Raman microprobe spectroscopy. *Adv Infrared Raman Spectrosc* **1981**, *7*, 223-282. (Ch 4)
29. Chase, DB; Rabolt, JF. *Fourier transform Raman spectroscopy; From concept to experiment.* Academic Press, New York, 1994.
30. Messerschmidt, RG; Chase DB. Fourier transform Raman microscopy: Discusion and preliminary results. *Appl Spectrosc* **1989**, *43*, 11-15.
31. Blaha, JJ. Raman microprobe spectroscopic analysis. *Vib Spectra Struct* **1981**, *10*, 227-282.
32. Katon, JE; Pacey, GE; O'Keefe, JF. Vibrational molecular microspectroscopy. *Anal Chem* **1986**, *58*, 465A-481A.
33. Messerschmidt, RG; Harthcock, MA, eds. *Infrared Microspectroscopy: Theory and Applications.* Marcel Dekker, New York, 1988.
34. Huong, PV. Raman spectroscopy for biological applications, in Analytical Raman Spectroscopy. Grasselli, JG; Bulkin, BJ, eds. Wiley, New York, **1991**, Ch 11, 397-423.
35. Humecki, HJ, ed. *Practical guide to infrared microspectroscopy*, Marcel Dekker, Inc., New York, NY, 1995.
36. Wopenka, B; Pasteris, JD. Limitations to quantitative analysis of fluid inclusions in geological samples by laser Raman microprobe spectroscopy. *Appl Spectrosc* **1986**, *40*, 144-151.
37. Wopenka, B; Pasteris, JD. Raman intensities and detection limits of geochemically relevant gas mixtures for a laser Raman microprobe. *Anal Chem* **1987**, *59*, 2165-2170.
38. Bartick, EG. Microscopy/infrared spectroscopy for routine sample sizes. *Appl Spectrosc* **1985**, *39*, 885-889.
39. Tungol, MW; Bartick, EG, Montaser, A. Forensic analysis of acrylic copolymer fibers by infrared microscopy. *Appl Spectrosc* **1993**, *47*, 1655-1658.

40. Shearer, JC; Peters, DC; Newton, GHT. FTIR in the service of art conservation. *Anal Chem* **1983**, *55*, 874A-880A.
41. Gerrard, DL; Maddams, WF. Polymer characterization by Raman spectroscopy. *Appl Spectrosc Rev* **1986**, *22*, 251-334.
42. Gerson, DJ; Chess, CA. in *Infrared Microspectroscopy: Theory and Applications*. Messerschmidt, RG; Harthcock, MA; eds. Marcel Dekker, New York, 1988, Chapter 5, pp. 73-83.
43. Colthup, NB. *Introduction to infrared and Raman spectroscopy*, 3rd ed. Academic Press, Boston, 1990.
44. Rochow, TG. *Introduction to microscopy by means of light, electrons, X-rays, or acoustics*. 2nd ed. Plenum Press, New York, 1994.
45. Reffner, JA; Martoglio, PA; Williams, GP. Fourier transform infrared microscopical analysis with synchrotron radiation: the microscope optics and system performance. *Rev Sci Instrum* **1995**, *66*, 1298-1302.
46. O'Leary, TJ; Engler, WF; Ventre, KM. Infrared microspectroscopy of human tissue. *Appl Spectrosc* **1989**, *43*, 1095-1097.
47. Lewis, EN; Kalasinsky, VF; Levin, IW. Development of near-infrared Fourier transform Raman spectroscopy for the study of biologically active molecules. *Appl Spectrosc* **1988**, *42*, 1188-1193.
48. Schrader, B. Chemical applications of Raman spectroscopy. *Angew Chem Int Edit* **1973**, *12*, 884-908.
49. Campion, A. Fluorescence-free scanning Raman spectroscopy. *J Am Chem Soc* **1988**, *110*, 408-410.
50. Treado, PJ; Morris, MD. Multichannel Hadamard transform Raman microscopy. *Appl Spectrosc* **1990**, *44*, 1-4.
51. Schwab, SD; McCreery, RL. Versatile, efficient Raman sampling with fiber optics. *Anal Chem* **1984**, *56*, 2199-2204.
52. Lewis, EN; Kalasinsky, VF; Levin, IW. Near-infrared Fourier transform Raman spectroscopy using fiber-optic assemblies. *Anal Chem* **1988**, *60*, 2658-2661.
53. Asher, SA. UV resonance Raman spectroscopy for analytical, physical, and biophysical chemistry. *Anal Chem* **1993**, *65*, 59A-66A.
54. Chang, RK; Furtak, TE; eds. *Surface Enhanced Raman Scattering*. Plenum Press, New York, 1982.
55. Asselin, KJ; Chase, B. FT-Raman spectroscopy at 1.339 micrometers. *Appl Spectrosc* **1994**, *48*, 699-701.
56. Harthcock, MA; Atkin, SC. in *Infrared Microspectroscopy: Theory and Applications*. Messerschmidt, RG; Harthcock, MA; eds. Marcel Dekker, New York, 1988, Chapter 2, pp. 21-39.
57. Harthcock, MA; Atkin, SC. Imaging with functional group maps using infrared microspectroscopy. *Appl Spectrosc* **1988**, *42*, 449-455.

58. Pell, RJ; McKelvy, ML; Harthcock, MA. Effective resolution enhancement of infrared microspectroscopic data by multiresponse nonlinear optimization. *Appl Spectrosc* **1993**, *47*, 634-642.
59. Treado, PJ; Levin, IW; Lewis, EN. Near-infrared acousto-optic filtered spectroscopic microscopy: A solid-state approach to chemical imaging. *Appl Spectrosc* **1992**, *46*, 553-559.
60. Treado, PJ; Levin, IW; Lewis, EN. Indium antimonide (InSb) focal plane array (FPA) detection for near-infrared imaging microscopy. *Appl Spectrosc* **1994**, *48*, 607-615.
61. Barry, B; Mathies, R. Resonance Raman microscopy of rod and cone photoreceptors. *J Cell Biol* **1982**, *94*, 479-482.
62. Loppnow, GR; Barry, BA; Mathies, RA. Why are blue visual pigments blue? a resonance Raman microprobe study. *Proc Natl Acad Sci USA* **1989**, *86*, 1515-1518.
63. Puppels, GJ; de Mul, FFM; Otto, C; Greve, J; Robert-Nicoud, M; Arndt-Jovin, DJ; Jovin, TM. Studying single living cells and chromosomes by confocal Raman microspectroscopy. *Nature* **1990**, *347*, 301-304.
64. Puppels, GJ; Garritsen, HSP; Sagers-Nolten, GMJ; De Mul, FFM; Greve, J. Raman microspectroscopic approach to the study of human granulocytes. *Biophys J* **1991**, *60*, 1046-1056.
65. Puppels, GJ; Ohninkhof, JHF; Sagers-Nolten, GMJ; Otto, C; de Mul, FFM; Greve, J. Laser irradiation and Raman spectroscopy of dingle living cells and chromosomes: sample degradation occurs with 514.5 nm but not with 660 nm laser light. *Exp Cell Res* **1991**, *195*, 361-367.
66. Dong, A; Messerschmidt, RG; Reffner, JA; Caughey, WS. Infrared spectroscopy of a single cell - the human erythrocyte. *Biochem Biophys Res Commun* **1987**, *156*, 752-756.
67. Sureau, F; Chinsky, L; Amirand, C; Ballini, JP; Duquesne, M; Laigle, A; Turpin, PY; Vigny, P. An ultraviolet micro-Raman spectrometer: Resonance Raman spectroscopy within single living cells. *Appl Spectrosc* **1990**, *44*, 1047-1051.
68. Wong, PTT; Rigas, B. Infrared spectra of microtome sections of human colon tissues. *Appl Spectrosc* **1990**, *44*, 1715-1718.
69. Wong, PTT; Wong, RK; Caputo, TA; Godwin, TA; Rigas B. Infrared spectroscopy of exfoliated human cervical cells: Evidence of extensive structural changes during carcinogenesis. *Proc Natl Acad Sci USA* **1991**, *88*, 10988-10992.
70. Wong, PTT; Wong, RK; Fung, MFK. Pressure tuning FT-IR study of human cervical tissues. *Appl Spectrosc* **1993**, *47*, 1058-1063.
71. Wong, PTT; Lacelle, S; Yazdi, HM. Normal and malignant human colonic tissues investigated by pressure tuning FT-IR spectroscopy. *Appl Spectrosc* **1993**, *47*, 1830-1836.

72. Redd, DCB; Feng, ZC; Yue, KT; Gansler, TS. Raman spectroscopic characterization of human breast tissues: implications for breast cancer diagnosis. *Appl Spectrosc* **1993**, *47*, 787-791.
73. Frank, CJ; Redd, CB; Gansler, TS; McCreery, RL. Characterization of human breast biopsy specimens with near-IR Raman spectroscopy. *Anal Chem* **1994**, *66*, 319-326.
74. Benedetti, E; Palatresi, MP; Vergamini, P; Papineschi, F; Andreucci, MC; Spremolla, G. Infrared characterization of nuclei isolated from normal and leukemic (B-CLL) lymphocytes: Part III. *Appl Spectrosc* **1986**, *40*, 39-43.
75. Benedetti, E; Teodori, L; Trinca, ML; Vergamini, P; Salvati, F; Mauro, F; Spremolla, G. A new approach to the study of human solid tumor cells by means of FT-IR microspectroscopy. *Appl Spectrosc* **1990**, *44*, 1276-1280.
76. Todd, EA; Morris, MD. Micron surface-enhanced Raman spectroscopy of intact biological organisms and model systems. *Appl Spectrosc* **1994**, *48*, 545-548.
77. Dalterio, RA; Nelson, WH; Britt, D; Sperry, J; Purcell, FJ. A resonance Raman microprobe study of chromobacteria in water. *Appl Spectrosc* **1986**, *40*, 271-272.
78. Dalterio, RA; Baek, M; Nelson, WH; Britt, D; Sperry, JF; Purcell, FJ. The resonance Raman microprobe detection of single bacterial cells from a chromobacterial mixture. *Appl Spectrosc* **1987**, *41*, 241-244.
79. Baek, M; Nelson, WH; Britt, D; Sperry, JF. UV-excited resonance Raman spectra of heat denatured lysozyme and *Staphylococcus epidermidis*. *Appl Spectrosc* **1988**, *42*, 1312-1314.
80. Clarke, RH; Hanlon, EB; Isner, JM; Brody, H. Laser Raman spectroscopy of calcified atherosclerotic lesions in cardiovascular tisue. *Appl Optics* **1987**, *26*, 3175-3177.
81. Tomazic, BB; Etz, ES; Brown, WE. Nature and properties of cardiovascular deposits. *Scanning Microsc* **1987**, *1*, 95-105.
82. Klug, DD; Singleton, DL; Walley, VM. Laser Raman spectrum of calcified human aorta. *Lasers Surg Med* **1992**, *12*, 13-17.
83. Baraga, JJ; Feld, MS; Rava, RP. *In situ* optical histochemistry of human artery using near infrared Fourier transform Raman spectroscopy. *Proc Natl Acad Sci USA* **1992**, *89*, 3473-3477.
84. Kodali, DR; Small, DM; Powell, J; Krishnan, K. Infrared micro-imaging of atherosclerotic arteries. *Appl Spectrosc* **1991**, *45*, 1310-1317.
85. Choo, L-P; Jackson, M; Halliday, WC; Mantsch, HH. Infrared spectroscopic characterisation of multiple sclerosis plaques in the human central nervous system. *Biochim Biophys Acta* **1993**, *1182*, 333-337.
86. Fabian, H; Choo, L-P; Szendrei, GI; Jackson, M; Halliday, WC; Otvos, L Jr; Mantsch, HH. Infrared spectroscopic characterization of Alzheimer plaques. *Appl Spectrosc* **1993**, *47*, 1513-1518.

87. LeVine, SM; Wetzel, DL. Analysis of brain tissue by FT-IR microspectroscopy. *Appl Spectrosc Rev* **1993**, *28*, 385-412.
88. Wetzel, DL; LeVine, SM. *In situ* FT-IR microspectroscopy and mapping of normal brain tissue. *Spectrosc* **1993**, *8*, 40-45.
89. LeVine, SM; Wetzel, DL. *In situ* chemical analysis of brain tissue by Fourier transform infrared microspectroscopy. *Neuroprotocols* **1994**, *5*, 63-71.
90. Levine, SM; Wetzel, DL; Eilert, AJ. Neuropathology of twitcher mice: examination by histochemistry, immunohistochemistry, lectin histochemistry, and Fourier transform infrared microspectroscopy. *Int J Dev Neurosci* **1994**, *12*, 275-288.
91. Levine, SM; Wetzel, DL. *In situ* chemical analyses from frozen tissue sections by Fourier transform infrared microspectroscopy: examination of the white matter exposed to extravasated blood in the rat brain. *Am J Pathol* **1994**, *145*, 1041-1047.
92. Kodati, VR; Tu, AT. Raman spectroscopic identification of cystine-type kidney stone. *Appl Spectrosc* **1990**, *44*, 837-839.
93. Sudlow, K; Woolf, A. Identification of renal calculi by their Raman spectra. *Clin Chim Acta* **1991**, *203*, 387-394.
94. Kodati, VR; Tu, AT; Turumin, JL. Raman spectroscopic identification of uric-acid-type kidney stone. *Appl Spectrosc* **1990**, *44*, 1134-1136.
95. Kodati, VR; Tomasi, GE; Turumin, JL; Tu, AT. Raman spectroscopic identification of calcium-oxalate-type kidney stone. *Appl Spectrosc* **1990**, *44*, 1408-1411.
96. Kodati, VR; Tomasi, GE; Turumin, JL; Tu, AT. Raman spectroscopic identification of phosphate-type kidney stone. *Appl Spectrosc* **1991**, *45*, 581-583.
97. Hong, TDN; Phat, D; Plaza, P; Daudon, M; Dao, NQ. Identification of urinary calculi by Raman laser fiber optics spectroscopy. *Clin Chem* **1992**, *38*, 292-298.
98. Kodati, VR; Tu, AT; Nath, R; Turumin, JL. Analysis of urinary calculi of mixed and unusual composition: Raman spectroscopic investigation. *Appl Spectrosc* **1993**, *47*, 334-337.
99. Daudon, M; Protat, MF; Reveillaud, RJ; Jaeschke-Boyer, H. Infrared spectrometry and Raman microprobe in the analysis of urinary calculi. *Kidney Int* **1983**, *23*, 842-850.
100. Hong, TDN; Phat, D; Plaza, P; Daudon, M; Dao, NQ. Identification of urinary crystals by Raman laser fiber optics spectroscopy. *Clin Chem* **1992**, *38*, 292-298.
101. Johnson, FB; Kalasinsky, VF. Unpublished results.
102. Martoja, R; Melieres, F; Raynaud, C; Truchet, M. Donnes physico-chimiques et cristallographiques sur les calculs renaux de la nephropathie

au chlorure mercurique d'un mammifere, le lapin. *C R Acad Sci Paris, Ser III* **1981**, *292*, 857-862. [Physico-chemical and crystallographic data on renal calculi from mercuric chloride nephropathy in a mammal, the rabbit]

103. Martoja, R; Truchet, M; Bouquegneau, J-M. Une nephropathie provoquee par le cadmium chez l'Anguille adaptee a l'eau de mer (Teleosteen). *C R Acad Sci Paris, Ser III* **1982**, *295*, 369-374. [Cadmium-induced nephropathy in eels adapted to sea water (teleosts)]

104. Zheng, S; Tu, AT. Spectroscopic identification of gallstone. *Appl Spectrosc* **1987**, *41*, 696-697.

105. Ishida, H; Kamoto, R; Uchida, S; Ishitani, A; Ozaki, Y; Iriyama, K; Tsukie, E; Shibata, K; Ishihara, F; Kameda, H. Raman microprobe and Fourier transform-infrared microsampling studies of the microstructure of gallstones. *Appl Spectrosc* **1987**, *41*, 407-412.

106. Keen, CE; Crocker, PR; Brady, K; Hasan, N; Levison, DA. Calcium pyrophosphate dihydrate deposition disease: morphological and microanalytical features. *Histopathol* **1991**, *19*, 529-536.

107. Maugars, YM; Peru, LF; El Messaoudi, B; Michaud, GO; Berthelot, J-MM; Prost, AM; Daculsi, G. Pelvic pseudotumoral calcium pyrophosphate dihydrate deposition: an ultrastructural study. *J Rheumatol* **1994**, *21*, 573-576.

108. McGill, N; Dieppe, PA; Bowden, M; Gardiner, DJ; Hall, M. Identification of pathological mineral deposits by Raman microscopy. *Lancet* **1991**, *337*, 77-78.

109. Centeno, JA; Ishak, KG; Mullick, FG; Gahl, WA; O'Leary, TJ. Infrared microspectroscopy and laser Raman microprobe in the diagnosis of cystinosis. *Appl Spectrosc* **1994**, *48*, 569-572.

110. Mendelsohn, R; Hassankhami, A; DiCarlo, E; Boskey, A. FT-IR microscopy of endochondral ossification at 20 u spatial resolution. *Calcif Tissue Int* **1989**, *44*, 20-24.

111. Centeno, JA; Kalasinsky, VF; Johnson, FB; Vinh, TN; O'Leary, TJ. Fourier transform infrared microscopic identification of foreign materials in tissue sections. *Lab Invest* **1992**, *66*, 123-131.

112. Fenton, JJ; Pryzygodski, RM; Johnson, FB; Kalasinsky, VF; Al-Dayel, F; Travis, WD. Sodium polystyrene sulfonate (Kayexalate) aspiration: Histologic appearance and infrared microspectrophotometric analysis of two cases. *Arch Pathol* **1995**, *XX*, 0000-0000.

113. De Mul, FFM; Buiteveld, H; Lankester, J; Mud, J; Greve, J. Raman microspectroscopy in human pathology. *Hum Pathol* **1984**, *15*, 1062-1068.

114. Buiteveld, H; De Mul, FFM; Mud, J; Greve, J. Identification of inclusions in lung tissue with a Raman microprobe. *Appl Spectrosc* **1984**, *38*, 304-306.

115.Kessler, DA. The basis for the FDA's decision on breast implants. *N Engl J Med* 1992, *326*, 1713-1715.
116.Delage, C; Shane, JJ; Johnson, FB. Mammary silicone granuloma. Migration of silicone fluid to abdominal wall and inguinal region. *Arch Dermatol* **1973**, *108*, 104-107.
117.Smahel, J; Sell, J. Contamination of human tissues with silicon: location and detection. *Mater Tech* **1978**, *6*, 51-54.
118.Smahel, J. Foreign material in the capsules around breast prostheses and the cellular reaction to it. *Br J Plast Surg* **1979**, *32*, 35-42.
119.Gayou, RM. A histological comparison of contracted and non-contracted capsules around silicone breast implants, *Plast Reconst Surg* **1979**, *63*, 700-707.
120.Frick, R; Baudisch, H. Physikalisch-chemischer Nachweis von intravasalem Silikon in Hirn und Nieve. *Beitr Pathol Bd* **1973**, *149*, 39-46. [Physico-chemical determination of intravascular silicone in brain and kidney.]
121.Kossovsky, N; Millett, DE; Wrobleski, DA. Fourier transform infrared spectroscopic analysis of organic oil mastitis. *Am J Clin Pathol* **1992**, *97*, 34-39.
122.Centeno, JA; Johnson, FB. Microscopic identification of silicone in human breast tissues by infrared microspectroscopy and X-ray microanalysis. *Appl Spectrosc* **1993**, *47*, 341-345.
123.Hardt, NS; Yu, LT; La Torrre, G; Steinbach, B. Fourier transform infrared microspectroscopy used to identify foreign materials related to breast implants. *Mod Pathol* **1994**, *7*, 669-676.
124.Centeno, JA; Luke, JL; Kalasinsky, VF; Johnson, FB; Mullick, FG; Panos, R. Vibrational microspectroscopy identification of pathologic inclusions in fibrous capsules associated with breast implants. *Plast Reconstr Surg* **1995**, *XX*, 0000-0000.
125.Luke, JL; Kalasinsky, VF. Unpublished results.
126.Frank, CJ; McCreery, RL; Redd, DCB; Gansler, TS. Detection of silicone in lymph node biopsy specimens by near-infrared Raman spectroscopy. *Appl Spectrosc* **1993**, *47*, 387-390.
127.Cai, M-Z; Kuck, JFR; Yu, N-T. Galactose-induced cataract in rat: Raman detection of sulfhydryl decrease and water increase along an equatorial diameter. *Exp Eye Res* **1989**, *49*, 531-541.
128.Bot, ACC; Huizinga, A; De Mul, FFM; Vrensen, GFJM; Greve, J. Raman microspectroscopy of fixed rabbit and human lenses and lens slices: New potentialities. *Exp Eye Res* **1989**, *49*, 161-169.
129.Huizinga, A; Bot, ACC; De Mul, FFM; Vrensen, GFJM; Greve, J. Local variation in absolute water content of human and rabbit eye lenses measured by Raman microspectroscopy. *Exp Eye Res* **1989**, *48*, 487-496.

130.Siebinga, I; Vrensen, GFJM; De Mul, FFM; Greve, J. Age-related changes in local water and protein content of human eye lenses measured by Raman microspectroscopy. *Exp Eye Res* **1991**, *53*, 233-239.
131.Shun-Shin, GA; Vrensen, GFJM; Brown, NP; Willekens, B; Smeets, MH; Bron, AJ. Morphologic characteristics and chemical composition of Christmas tree cataract. *Invest Ophthalmol Vis Sci* **1993**, *34*, 3489-3496.
132.Kalasinsky, KS; Magluilo, J Jr; Schafer, T. Hair analysis by infrared microscopy for drugs of abuse. *Forensic Sci Int* **1993**, *63*, 253-260.
133.Kalasinsky, KS; Magluilo, J Jr; Schafer, T. Study of drug distribution in hair by infrared microscopy visualization. *J Anal Toxicol* **1994**, *18*, 337-341.
134.Osborne, BG; Fearn, T. *Near infrared spectroscopy in food analysis.* Wiley, New York, 1986.
135.Wallon, J; Yan, SH; Tong, J; Meurens, M; Haot, J. Identification of breast carcinomatous tissue by near-infrared reflectance spectroscopy. *Appl Spectrosc* **1994**, *48*, 190-193.
136.Cassis, LA; Lodder, RA. Near-IR imaging of atheromas in living arterial tissue. *Anal Chem* **1993**, *65*, 1247-1256.
137.Puppels, GJ; Grond, M; Greve, J. Direct imaging Raman microscope based on tunable wavelength excitation and narrow-band emission detection. *Appl Spectrosc* **1993**, *47*, 1256-1267.
138.Morris, HR; Clifford, CH; Treado, PJ. Imaging spectrometers for fluorescence and Raman microscopy: acousto-optic and liquid crystal tunable filters. *Appl Spectrosc* **1994**, *48*, 857-866.
139.Pallister, DM; Morris, MD. Laser Koehler epi-illumination for Raman and fluorescence microscopic imaging. *Appl Spectrosc* **1994**, *48*, 1277-1281.
140.Lewis, EN; Levin, IW. Real-time, mid-infrared spectroscopic imaging microscopy using indium antimonide focal-plane array detection. *Appl Spectrosc* **1995**, *49*, 672-678.